ABSTRACT

Title of thesis: GRAMIAN-AWARE CLOSED LOOP FLIGHT CONTROL DESIGN FOR ENERGY HARVESTING THROUGH MODULATING DISTURBANCE SENSITIVITY

Utsav Saxena, Master of Science, 2017

Thesis directed by: Professor Imraan A. Faruque
Department of Aerospace Engineering

Many desired micro aerial vehicle missions are significantly larger than the mission endurance of the vehicles. Due to extreme constraints on size, weight and power available, small scale air vehicles are highly sensitive to atmospheric disturbance. This work introduces a control-theoretic framework that models the magnitude of the vehicle's disturbance sensitivity and observability in conjunction with each other under a gramian-based formulation. To implement atmospheric gust response modulatiom, a "gramian-aware" flight control law is designed using open loop plant models across various scales and assuming perfect gust measurement. Time-domain system identification was conducted using data collected from repeatable automated flights in a motion capture arena in order to derive the plant model. Closed-loop simulation results as well as experimental data modulating the plant using cruise speed are presented to illustrate that the gramian-based control laws can be utilized to facilitate atmospheric energy scavenging in gusting environments.

GRAMIAN-AWARE CLOSED LOOP FLIGHT CONTROL DESIGN FOR ENERGY HARVESTING THROUGH MODULATING DISTURBANCE SENSITIVITY

by

Utsav Saxena

Thesis submitted to the Faculty of the Graduate School of the
University of Maryland, College Park in partial fulfillment
of the requirements for the degree of
Master of Science
2017

Advisory Committee:
Dr. Imraan A. Faruque, Chair/Advisor
Dr. Derek A. Paley
Dr. Inderjit Chopra

Acknowledgments

I am indebted to all the individuals who have enabled and influenced me towards completing this thesis and ensuring that my graduate school memories remain the most challenging and simultaneously fulfilling experience of my life.

First and foremost I would like to thank my advisor Dr. Imraan Faruque for extending this incredible opportunity to work with him in some of the most exciting theoretical and application areas in the field of controls and automation. His passion and drive in the field infected me with the same as I got on board and there was never a moment where his immediate guidance and expertise regarding results and challenges were unavailable. It has been a source of great pleasure and support to work with such a motivated advisor.

I would also like to thank the U.S. Army Research Laboratory team at Aberdeen Proving Grounds for their funding as well as regular advising and providing the logistical support to carry out the experimental work presented here. Dr. Christopher Kroninger and Dr. Michael R. Dorothy provided their invaluable inputs and interpretations throughout this project. Dr. John Hrynuk's expertise with wind-tunnel testing came as a tremendous resource towards characterizing crucial components of the experimental setup. I would also like to thank Howard Carpenter's indispensable resourcefulness in facilitating and being involved through every aspect of execution of experimental validations.

I am further grateful to my committee members Dr. Derek A. Paley and Dr. Inderjit Chopra for agreeing to serve on my thesis committee and review this effort.

Further, it has been an honor to be able to learn some of the most rigorous and constructive instructional material from all the professors at the University of Maryland's Aerospace Engineering department, and be able to incorporate crucial pieces of it towards this work. The help I received from current and former labmates like Dr. Badri Ranganathan, Dr. Lina Castano and Dr. Mac MacFarlane on a range of topics from the abstract concepts to experimental challenges has also been crucial towards completion of this work.

I recall my undergraduate professors at the University of Florida, Dr. Prabir Barooah, Dr. Rick Lind, Dr. Subrata Roy, Dr. Norman Fitz-Coy and Dr. Mark Sheplak for sparking my initial interest in the field of controls research and motivating me towards pursuing higher learning in the field. I am also thankful to my former colleagues and mentors at Belcan and Pratt and Whitney like Robert Jamilla, Phillip Hoover, Dimitrios Panagoulias, Paul Russell, Alicia Joy Hollopeter, Derek Palm, Nick Bidgood, and several others, for the controls engineering expertise they provided me during my four years of industry experience prior to returning to school.

Finally I would like to thanks all my family who have been tremendous sources of support and inspiration all my life and particularly through this most challenging endeavour. My mother Dr. Rimjhim Banerjee-Batist and father Carlos Batist had shown by example from the trials and tribulations of reaching their own achievements that the path was challenging yet rewarding. My grandfather and retired mining engineer Shri Ashoke Kumar Banerji had always questioned me on a score of 99 out of 100 in mathematics exams, impressing upon me from childhood that

in the objective sciences, there is no room for imperfections. I am most indebted to my wife Parnika Salooja Saxena for her constant support throughout this whole period mentally, physically, emotionally and academically as well. She was generally my first audience for any of my presentations, while her high school math teaching career meant that I always had an available resource at home for the often rusty yet vital mathematical tools and concepts. A semester into my graduate school curriculum, our daughter Urvashi Saxena was born. I am grateful to her as well for being a constant source of bliss and joy since her arrival and to my in-laws Amita and Rajeev Salooja for their invaluable moral, emotional and logistical support through these demanding times.

My gratitude extends to all of the individuals mentioned above as well as several others whom I may not recall at the moment. Thank you all.

Table of Contents

List of Tables

List of Figures

List of Abbreviations

α	Angle of Attack
β	Angle of Sideslip
M	Total pitch moment
M_G	Gust Capture Metric
Δq	Change in pitch rate from steady-state condition
$\Delta \dot{q}$	Change in pitch acceleration from steady-state condition
$\Delta \theta$	Change in pitch angle from steady-state condition
Δu	Change in forward velocity from steady-state condition
$\Delta \dot{u}$	Change in forward acceleration from steady-state condition
Δw	Change in vertical velocity from steady-state condition
$\Delta \dot{w}$	Change in vertical acceleration from steady-state condition
X	Total forward force
X_c	Disturbance or controllability gramian
Y_o	Observability gramian
Z	Total vertical force

ARL	United States Army Research Laboratory
AVL	Athena Vortex Lattice
BNF	Bind And Fly
LTI	Linear Time Invariant
MAV	Micro-Aerial Vehicle
PWM	Pulse-Width Modulation
RMS	Root-mean square
SUAV	Small Unmanned Aerial Vehicle
UAV	Unmanned Aerial Vehicle

Chapter 1: Introduction

1.1 Motivation

Small unmanned aerial systems and micro aerial vehicles (MAVs) have been finding increasing application in a wide range of both civilian and military usage due to their portability and advances in microtechnology. Various niche areas ranging from precision agriculture [1] and wildlife research [2] to military reconnaissance for urban combat and counterterrorist operations [3] have increasingly incorporated these vehicles into their missions while simultaneously furthering the demand on the physical capacities of the vehicles. At the operational level, the physical constraints of size, weight and power remain the major contributing factor towards limiting mission endurance and range. A recent survey of small quadrotor applications by Mulgaonkar et al. [4] concluded that the battery is the most significant contributor to the vehicle mass, and therefore the flight time of the vehicle is closely linked with the mass and inertia of the vehicle.

Moreover, the mission endurance and vehicle stability of these systems can both be strongly affected by atmospheric gusts [5]. The scale and duration of these impactful gusts, as can be generated in narrow urban environments where such systems are desired for application, need not be noticeable even at a human level in

order to affect performance due to the vehicle's relatively small mass and inertia; thereby causing it to use its own energy to actively combat or reject the gust effects. Working within the physical constraints such as battery power and weight, innovative control methods may have a role in bringing about this desired improvement in endurance.

Previous work has investigated the effect of variables such as mass distribution or cruise speed on traditional flight control [6]. The goal in these studies has been flight stabilization and control, but at the small scale, gust rejection remains a major challenge. Recent and current work has produced methods of sensing atmospheric gusts [7] [8]. There is also potential for inertial sensing approaches that are able to measure motion caused by gusts. While accurate sensing of directionality and scale of these MAV-level impactful gust structures remains an active research area, the scope of this thesis considers the gust characteristic as a known quantity and investigates the impact of autonomous flight algorithms designed using an open loop vehicle dynamics model.

A gramian-based formulation of a well-characterized system can be used to understand a vehicle's gust response characteristics. Since a gust response gramian denotes the gust-sensitive and gust-resistant directions of a vehicle [9], a feedback controller that operates with knowledge of these directions may be able to dynamically actuate the vehicle and alter its gust response properties, thereby potentially taking advantage of the energy stored in the surrounding field. In this way, the controller may act to maximize the vehicle's response to favorable gusts, and minimize the same response to an unfavorable gust, resulting in an overall energy gain

or equivalently a minimized energy loss given environmental conditions.

1.2 Background Work

A basic explanation of the gramian framework utilized in this project follows through a definition of the disturbance and observability gramians. Consider a linearized time-invariant state-space model,

$$\dot{x} = Ax + Bu + Dg, \tag{1.1}$$

$$y = Cx, \tag{1.2}$$

where x contains all the states of the system, u has the control inputs to the system, g is the atmospheric disturbances to the vehicle, A is the plant dynamics matrix, B is the input-feedthrough matrix, C is the output matrix and D is the disturbance feedthrough matrix. If the controllability matrix of (A, D) is full rank, then the steady-state disturbance gramian X_c is the solution to the Lyapunov equation

$$AX_c + X_cA^* + DD^* = 0. \tag{1.3}$$

The steady state disturbance gramian gives a measure of the reachable space for unit-norm disturbance input acting on $t \in [-\infty, 0]$ in the form of the disturbance ellipsoid as defined by the eigenvectors and eigenvalues of $X_c^{\frac{1}{2}}$. In Fig. 1.1, μ_i and ν_i are the eigenvalues and eigenvectors, respectively of $X_c^{\frac{1}{2}}$. Thus, the disturbance ellipsoid in Fig. 1.1 illustrates which states are more or less sensitive to a disturbance [10]. Note that since the input is considered to be unit-norm, the disturbance

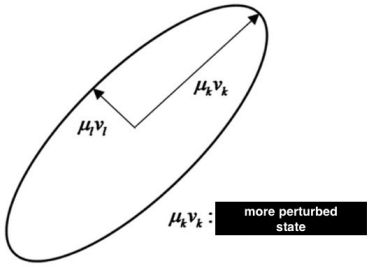

Figure 1.1: The disturbance gramian ellipsoid encodes the magnitudes and directionality of gust response sensitivity.

gramian in itself and its ellipsoid representation is insensitive to sign changes in input.

If the observability matrix of (A, C) is full rank, the observability gramian Y_o maps a unit state input at $t \in [0, \infty]$ and is the Lyapunov solution of:

$$A^* Y_o + Y_o A + C^* C = 0. \tag{1.4}$$

The observability gramian also has its own ellipsoid, defined by the eigenvectors and eigenvalues of $Y_o^{\frac{1}{2}}$. This ellipsoid's size and direction provides insight into the strength and weakness of the observability of the respective states.

Gusts, described as an unsteady airflow consisting of mixing of discrete bursts and continuous turbulence, have been recognized for their negative impact on aircraft stability and performance from the beginning days of flight. A major part of the extant gust characterization work has focussed in the domain of large manned aircraft, with development of the Von Karman and Dryden models [11] for upper atmosphere flight, and only some extension to near-ground effects as necessitated by landing and takeoff considerations. For the applications considered for MAV's and

SUAV's, it has been recognized that the level of gust characterization, at the applicable low altitudes and slow flight speeds resulting in much higher proportion for the spatial turbulence to incoming flight velocity vector, is still in its infancy [12]. While early characterization and mitigation strategies attempted to simply scale down the high-altitude high-Reynolds number knowledge in linear fashion resulting in poor agreement with flight data [13], more recent high frequency and tighter grid resolution measurements at the MAV scale [14] [15] [16] have allowed for better insight into the path forward and challenges for proper gust handling. A subset of the Beaufort scale [17] of gust classification is provided below in Table 1.1, with the understanding that the majority of MAV and SUAV applications of interest are from Level 0 till Level 4.

Level	Wind Speed (m/s)	Description
0	<0.3	Calm
1	0.3-1.59	Light Air
2	1.6-3.4	Light Breeze
3	3.4-5.4	Gentle Breeze
4	5.5-7.9	Moderate Breeze

Table 1.1: Subset of the Beaufort scale of interest to MAV and SUAV applications.

A variety of control strategies have been suggested for handling gusts at the MAV and SUAV scale. Accurate and advanced knowledge of ambient gust fields is crucial for an autonomous system to effectively modulate its response in order to maintain stability and prevent performance degradation [18] [19]. Advances in

material fabrication including smart structures has allowed for considering in-flight wing planform alterations (span, sweep, and chord), out-of-plane transformation (twist, dihedral/gull, and span-wise bending), and airfoil adjustment (camber and thickness) [20]. Dillsaver et. al. [21] varied structural stiffness parameters on a highly flexible aircraft as part of their closed-loop control to study and mitigate gust response. Biologically inspired strategies of passive wing-articulation have also been explored to indicate that such a method can increase robustness to gusts [22], while also developing saturation limits on said articulation beyond which a rigid platform performs better. Vance et. al. [23] noted that flapping wing mechanisms in honeybees in a coordinated movement involving both symmetric and asymmetric maneuvers added to passive aerodynamic damping in the insects and aiding in their gust mitigation performane. In another flapping wing mechanism study [24], the maximum gust tolerance in terms of mean speed is compared across different controllers and lateral gusts are found to be far more impactful than longitudinal gusts. Reducing gust susceptibility was also the goal of a study by Singh et. al [25] where different novel wing configurations ranging from hole in wings to elastically hinged spoilers and variable dihedral angles were compared to each other in development of a gust-resistant wing.

Previous work on gust responses of MAVs has identified disturbance gramians and sought to attenuate gusts by juxtaposing the disturbance-sensitivity space with the controllable space via the aforementioned eigenanalysis as well as overall measures of size such as the Frobenius norm and determinants of the ellipsoids [26] [27]. While this approach helps understand the maximum extent of tolerable gust distur-

bances, there is no incorporation of directionality regarding whether the gust input is in a direction deemed favorable from an energy standpoint of the vehicle or not. From a gain selection perspective, previous work has applied empirical analysis approaches towards extracting atmospheric energy. Langelaan [28] [29] conducted a numerical optimization over an ensemble of flights, each over a fixed gust field, to identify the altitude-maximizing control gain. Patel et al. [30] compared an optimal set of gains, derived from a genetic optimization run in a simulated Dryden model environment. An analytic method of predicting the most efficient gains would provide a plant-model-centric insight into gust-capturing algorithms. The goal here is to utilize the gramian framework to take advantage of the gusts when possible by incorporating this knowledge of directionality and applying it over a range of gramian-formulations for the vehicle as can be achieved by the controller.

Since the premise of this work builds upon the gramian framework, system identification has played a vital role in the development of the theory as appropriate models are necessary to compute meaningful gramians. The goal of system identification is to derive a mathematical representation of the vehicle to best explain its unforced and forced dynamics [31]. An overview of the system identification process is illustrated in Fig. 1.2 [32]. The first step of model postulation consists of determining the kind of model to be used to define the dynamics. This depends on a number of items ranging from a priori knowledge of the system to ultimately the level of fidelity desired. Generally for conventional fixed-wing aircraft, this means expressing the aerodynamic forces and moments in terms of linear expansions, polynomials, or polynomial spline functions in the states and controls with time-invariant

coefficients. Empirical databases such as DATCOM [33] or vortex-lattice methods like Athena Vortex Lattice [34] may be used as a resource for an initial idea regarding the linearized model structure of aircraft near a particular flight condition. Due to the low Reynolds number regime of MAV's and SUAV's, only the larger end of SUAV's like the Apprentice [35] or UltraStick 25E [36] may yield accurate models from such methods, but at smaller levels, the limitations to such an approach become apparent [37]. Ultimately regardless of model size, experimental identification via flight trial remains the most accurate method of deriving a system model.

As a result, the flight experiment necessitates appropriate design to generate the input data for system identification. This includes selection of instrumentation system, flight condition and aircraft configuration specifications, and control inputs to facilitate the maneuvers in the aircraft and excite its various modes for identification. The goal here is to identify the system with high accuracy and repeatability as efficiently as possible. The optimal control input that maneuvers the aircraft in such a manner so as to allow for identification is a well investigated topic [38] [39]. A number of options ranging from doublets to sinusoidal frequency sweeps and chirp signals of varying amplitudes and frequencies can be considered based on the platform and measurement constraints.

Then using the measured data from the experiments, a data compatibility analysis is applied to verify accuracy. This step includes state estimation, estimation of instrumentation errors and sensor biases, and a comparison of reconstructed responses with measured responses. It becomes vital to address outliers and missing data in this step as well. After identifying the input and output data, the model

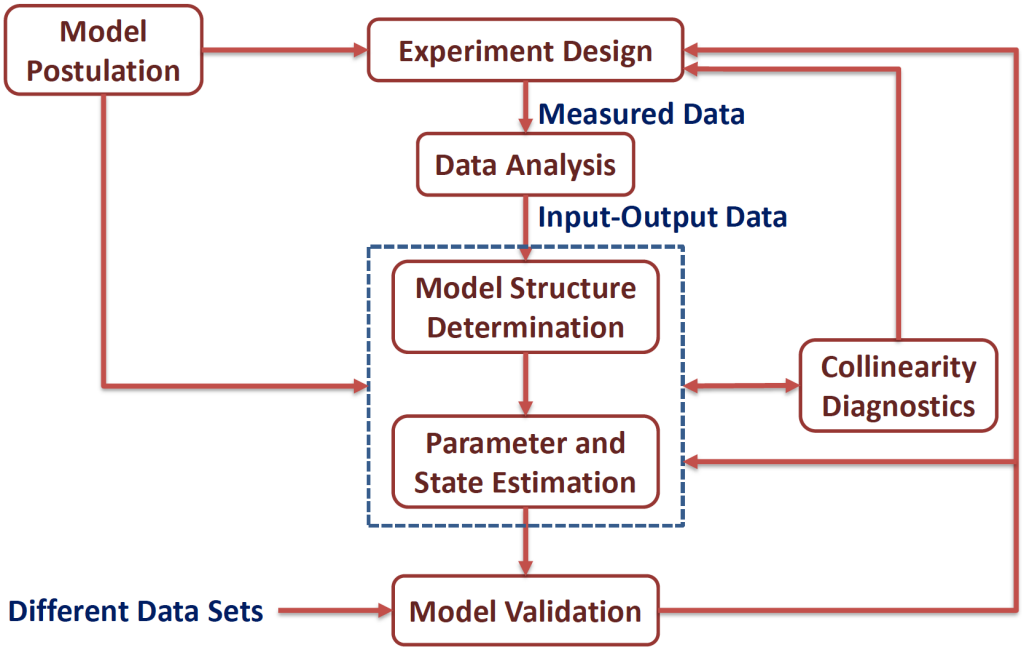

Figure 1.2: An overview of the system identification process.

structure is determined according to three classes [40], Bayesian, Fisher or Least-Squares. The objective of the parameter estimation is to find values of unknown coefficients θ from noisy measurements z and known inputs u. Regardless of whether a linear model of the form,

$$z = H\theta + v, \tag{1.5}$$

or a non-linear form is used

$$z = h(\theta) + v, \tag{1.6}$$

the three model structures treat the parameters θ and v uniquely. For the Bayesian model, θ is a vector of random variables with a probability density and v is a random vector with a probability density. In the Fisher model, θ is no longer random and is just a vector of unknown parameters while v is a random vector with a probability density like in the Bayesian model. Finally in the Least Squares model, θ is a vector of unknown parameters and v is a random vector of measurement noise. The Least Squares model operates on the idea of minimizing a cost function that penalizes the error sum squared. As a result this model tends to generate a lower variance but possibly a higher bias due to overfitting a particular trial. For inputs vectorized in time history as X and outputs Y related by

$$Y = X\theta \tag{1.7}$$

the coefficients can be estimated in the least-squares model from

$$\hat{\theta} = (X^T X)^{-1} X^T Y. \tag{1.8}$$

Collinearity diagnostics can be taken on the data to gauge the quality of the estimate from various statistical metrics like autocorrelation in the residuals, F-statistic,

collinearity between input and output. Generally these are small enough if the design of experiment and model postulation and structure determination were not too inaccurate. However, if sufficient collinearity exists, model term predictions can be inaccurate. This step helps determine corrective action if necessary.

The final step in system identification is model validation. This step determines how good the model is. The parameters must have physically reasonable values in terms of magnitudes and signs, there needs to be acceptable accuracy, and fair prediction capability from using different data sets, preferably with different control input profiles. Although this is the last step in model development, it may trigger an iteration if the identified model has poor prediction capability.

1.3 Problem Formulation

Given that the gramians contain information regarding the strength and weakness of reachability and observability from a prior knowledge of a given UAV platform's plant and input-feedthrough characteristics, this thesis develops a controller algorithm that modulates the disturbance sensitivity based on the aforementioned information and knowledge of whether the ambient gust field is favorable or not. For the purposes of validation by simulation and flight trials, a vertical gust section will be considered, and capacity for energy harvesting from said gust will be quantified by the metric of net altitude gain. The effectiveness of such a "gramian-aware" controller will be juxtaposed with a baseline controller, i.e. one that does not modulate the plant at all. Modulating the plant in the gramian-aware manner can be imple-

mented across several flight and vehicle-related factors, such as cruise speed, wing area, closed-loop gain selection, center of gravity location, etc. This work considers the effect of modulating cruise speed and closed-loop gain selection, and draws conclusions regarding this gramian-based approach towards energy harvesting.

1.4 Contributions

With the postulation of a "gust capture metric" discussed in detail in Chapter 2, this thesis develops a comprehensive method for using the information contained within a vehicle's gramians to build an atmospheric energy scavenging algorithm which would have significant impact upon vehicle energy, particularly at the small UAV and MAV level. Instead of attempting to attenuate gusts of both favorable and unfavorable type, the information encoded in this gramian-based approach incorporates directionality into the otherwise directionally-blind gramian framework in order to maximize energy gain in favorable gusts and attenuate the impact only of unfavorable gusts by modulating the plant accordingly. While the results from performing this modulation using cruise speed appear intuitive, the application using gain selection highlights the theoretical insight this approach develops towards atmospheric energy harvesting.

1. A method of quantifying the directional gust response for control uses by defining a gust capture metric.

2. An understanding of the variation of gust sensitivity information encoded within gramians with plant model parameters.

3. A gust response control strategy using cruise speed.

4. A theoretical, simulated, and experimental investigation of a problem using cruise speed variation.

5. A theoretical and simulated investigation of gain scheduling approaches to gust response.

1.5 Outline of Thesis

In Chapter 2, a more in-depth look is taken into gramian theory. The implications behind the controllability and observability gramians and their utilization across the field of controls and gust response work till date is noted. Then the "gust capture metric" M_G as a tool for development of the "gramian-aware" controller which seeks to extract atmospheric energy from gusts is presented. There is also a discussion about the Hankel operator in this chapter as it serves as the inspiration towards M_G.

In Chapter 3, a small UAV Night Vapor BNF is presented for analysis for a gramian-aware control law that modulates cruise speed. First, the results of system identification from flight are presented in order to arrive at the longitudinal linear-time invariant model of the aircraft. Then, simulation results over an idealized gust field consisting of equal and opposite magnitude step-input gusts are considered. Following that experimental validation work is presented. First, a custom-built gust generator apparatus is discussed, and then the results from flight trials are given. The gramian-aware controller's capacity to harness atmospheric energy in

the form of altitude gain by modulating its cruise speed is discussed.

In Chapter 4, five different longitudinal linear-time invariant models of varying sizes are considered for a gramian-aware control law that modulates closed-loop gains. The models are then simulated over similar idealized gust fields consisting of equal lengths of updrafts and downdrafts as in the previous chapter. The gramian-aware modulates its closed loop gains according to updraft or downdraft whereas the conventional controller flies over both sections with the same gains. Once again, the gramian-aware controller's capacity to harness atmospheric energy in the form of altitude gain via gain selection is discussed.

In Chapter 5, conclusions are drawn from the overall effort outlined throughout this thesis. Further expansions of the application of the theory developed here are considered as well as the challenges likely to arise as a result and potential methods of resolving them.

Chapter 2: Gramian Analysis and Gust Capture Metric Derivation

2.1 Gramian Theory

A gramian matrix $G = [g_{ij}] \in M_k$ of the vectors $v_1, ...v_k$ is defined by the inner product space of the respective vectors as $g_{ij} = \langle v_j, v_i \rangle$ [41]. As a result, a gramian matrix is always positive semi-definite. Further, if $v_1, ...v_k$ are linearly independent vectors, the gramian is non-singular and hence positive-definite. In application to linear control theory, a controllability gramian X_c exists for a controllable system [42] since it defines the control input that drives the system from x_i to x_f in finite time as seen in Fig. 2.1. Consider a general system dynamics model linearized about an equilibrium point of the form,

$$\dot{x}(t) = A(t)x(t) + B(t)u(t), \tag{2.1}$$

$$y(t) = C(t)x(t) + D(t)u(t), \tag{2.2}$$

where x and y represent the states and outputs of the system respectively. $A(t)$ is the open-loop plant, $B(t)$ is the control input feedthrough, $C(t)$ is the observer on the states and $D(t)$ is the feedforward of the control input directly onto the output. Further define a state transition matrix as one that defines the current state in terms

of the initial state as a solution to a homogeneous application of Equation (2.1),

$$x(t) = \Phi(t, t_i)x_i. \tag{2.3}$$

Then the control input,

$$u(\tau) = B^T(\tau)\Phi^T(t_f, \tau)X_c^{-1}(t_i, t_f)[x_f - \Phi(t_f, t_i)x_i], \tag{2.4}$$

steers the system from x_i to x_f in finite time t_f, where

$$X_c(t_i, t) = \int_{t_i}^{t} \Phi(t, \tau)B(\tau)B^T(\tau)\Phi^T(t, \tau)d\tau. \tag{2.5}$$

X_c is positive semi-definite from its definition, and if invertible or positive-definite, then controllability of the system or the ability to drive the system to any final state from the current state in finite time is guaranteed. Controllability gramians have the same implications for non-linear system models as well but they require the solution to a Hamilton-Jacobi partial differential equation and a nonlinear Lyapunov equation or a nonlinear Sylvester equation [43]. Due to non-feasibility of solutions for large-scale systems, non-linear analysis uses an empirical approach by systematically averaging gramians over a set of linearized regions.

If the general linear system is further simplified to a linear time-invariant (LTI) model, then [44]

$$\Phi(t, \tau) = e^{A(t-\tau)}, \tag{2.6}$$

with $\tau \in (t_i, t_f)$ and Equation (2.5) simplifies to [45]

$$X_c(0, t_f) = \int_0^{t_f} e^{A\sigma}BB^T e^{A^T\sigma}d\sigma, \tag{2.7}$$

with $t_i = 0$ and $\sigma = t_f - \tau$. In fact, by defining $X_c(t) = X_c(t, t_i)$, the following differential equation results,

$$\dot{X}_c(t) = A(t)X_c(t) + X_c(t)A^T(t) + B(t)B^T(t), \tag{2.8}$$

with the constraint $X_c(t = t_i) = 0$. For an LTI system with all eigenvalues of A in the left-half plane, this reduces to

$$\lim_{t\to\infty} X_c(t) = X_{c,ss} = constant, \tag{2.9}$$

and $X_{c,ss}$ is the Lyapunov solution of

$$AX_{c,ss} + X_{c,ss}A^T = -BB^T. \tag{2.10}$$

The controllability gramian has its implications in terms of defining the input that steers the system from initial to final point in finite time and thus towards controllability of the system at large. Dual to this, there is also the observability gramian formulation which, if it exists, implies that the evolution of the states in past time can be reconstructed from the current output and knowledge of the past input. As a result, if the initial states can be reconstructed from

$$x_i = Y_o^{-1}(t_i, t_f) \int_{t_i}^{t_f} \Big[y(t) - D(t)u(t) - \int_{t_i}^{t} C(t)\Phi(t, \tau)B(\tau)u(\tau)d\tau \Big] dt, \tag{2.11}$$

or in other words if the observability gramian $Y_o(t_i, t_f)$ is invertible, then the system is observable. Now the observability gramian is also at least positive semi-definite from definition,

$$Y_o(t_i, t_f) = \int_{t_i}^{t_f} \Phi^T(t, t_i)C^T(t)C(t)\Phi(t, t_i)dt, \tag{2.12}$$

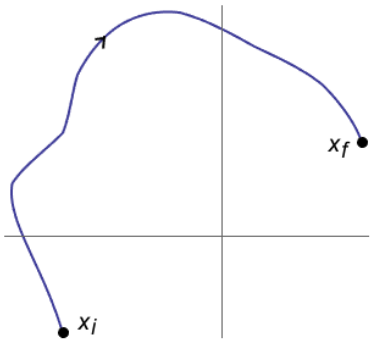

Figure 2.1: Evolution of final states and construction of initial states defined by controllability and observability gramians respectively.

therefore invertibility implies that existence of a positive-definite observability gramian signifies an observable system. Here also, there are nonlinear observability gramians with similar challenges and empirical observability gramians used as a compromise between the nonlinear and linear analyses. Considering an LTI formulation, this simplifies to

$$Y_o(0, t_f) = \int_0^{t_f} e^{A^T\sigma} C^T C e^{A\sigma} d\sigma, \tag{2.13}$$

and the steady-state observability gramian becomes the solution to the following Lyapunov formulation

$$A^T Y_{o,ss} + Y_{o,ss} A = -C^T C. \tag{2.14}$$

Besides a simple binary understanding on controllability or observability given by the existence of positive-definite controllability and observability gramians, there is also numerical insight to be attained from various metrics on these gramians. Chapter 1 discussed how the ellipsoid representations of the gramians with their respective eigenvectors and eigenvalues give insight into the strength and weakness of controllability and observability of each state in the system [46] [47]. It is worthwhile

to consider a scalar metric to draw qualitative understanding regarding controllability and observability from these gramians [48]. The maximum eigenvalue of X_c^{-1} is one such measure, with the larger this value corresponding to poorer controllability in the respective eigenvector direction. Another such measure is the trace of the inverse $Tr(X_c^{-1})$ as it is related to the average value of the minimum control energy [49]. Yet one more commonly used scalar metric has been the determinant of the inverse $Det(X_c^{-1})$. Note that the determinant of the gramian, if positive-definite, quantifies the square of the volume of the parallelotope formed by the vectors of the gramian [50].

Previous research has utilized the insight from computed gramians in a variety of manners. Beck et. al. [51] utilized the existence and rank of structured controllability and observability gramians in uncertain dynamic models to treat reductibility and to develop insight into output feedback stabilization for uncertain systems via a separation argument to full information and full control problems. L_2 sensitivity minimization has also been considered from a gramian perspective by incorporating them into the iterative procedure to minimize L_2 sensitivity of a nominal system [52]. In the practical domain, Marx et. al. [53] developed a manner for ideal placement of sensors and actuators based on maximizing observability and controllability of a system respectively. Shaker et. al. [54] furthered this analysis of ideal sensor and actuator placement on open-loop unstable systems. Montagnier et. al [55] developed the time-varying gain on their feedback controller for a linear time-periodic system using the controllability gramian.

Since a control input u and a gust disturbance input g have the same type of

impact on the state dynamics as seen in Equation (1.1), the notion of the controllability gramian and its implications towards how controllable the system is can be translated in the gust input case as a disturbance gramian and easily the system is perturbed. While the subjective meaning changes from considering g as opposed to u as the input, the theory behind the controllability and disturbance gramians is uniform and has been treated as such in previous research as well [56].

2.2 Gust Capture Metric and Gramian-Aware Control Law

Considering a longitudinal LTI model for a UAV including the gust-feedthrough matrix D in the form of Equation (1.1) [57]

$$\begin{bmatrix} \dot{\Delta u} \\ \dot{\Delta w} \\ \dot{\Delta q} \\ \dot{\Delta \theta} \end{bmatrix} = \begin{bmatrix} X_u & X_w & 0 & -g \\ Z_u & Z_w & u_0 & 0 \\ M_u & M_w & M_q & 0 \\ 0 & 0 & 1 & 0 \end{bmatrix} \begin{bmatrix} \Delta u \\ \Delta w \\ \Delta q \\ \Delta \theta \end{bmatrix} + \begin{bmatrix} X_{thr} & X_{ele} \\ Z_{thr} & Z_{ele} \\ M_{thr} & M_{ele} \\ 0 & 0 \end{bmatrix} \begin{bmatrix} \delta_{thr} \\ \delta_{ele} \end{bmatrix} + \begin{bmatrix} -X_u & -X_w & 0 \\ -Z_u & -Z_w & -u_0 \\ -M_u & -M_w & -M_q \\ 0 & 0 & 0 \end{bmatrix} \begin{bmatrix} u_g \\ w_g \\ q_g \end{bmatrix}, \tag{2.15}$$

where the states u, w, q, θ refer to forward velocity, vertical velocity, pitch rate and pitch angle respectively, the control inputs are throttle and elevator, and the gust inputs are forward, vertical and rotational about the pitch axis. In order to consider a pure vertical gust, the second column of D is selected for the Lyapunov solution to Equation (1.3) to give the disturbance gramian. Similarly, with appropriate selection of

$$C = \begin{bmatrix} 0 & 1 & 0 & 0 \end{bmatrix}, \tag{2.16}$$

only the vertical velocity state is considered for the Lyapunov solution to Equation (1.4) to give the observability gramian.

As discussed in Chapter 1, a steady-state disturbance gramian encodes the overall disturbance sensitivity to a unit-norm input acting on the system, whereas a steady-state observability gramian traces the observability of a unit-norm initial state condition of the system. It is desirable to incorporate the information in both these gramians into a combined metric.

A "gust capture metric" M_G is defined as a measure for disturbance sensitivity to a unit norm gust disturbance in the unit norm state as

$$M_G = Y_o^{\frac{1}{2}} X_c^{\frac{1}{2}}. \tag{2.17}$$

As a result of using the appropriately selected D and C matrices, this work proposes the resultant M_G from Equation (2.17) as a measure of sensitivity of the Δw state alone to a purely vertical gust input.

Both Y_o and X_c are positive-definite symmetric matrices while the plant matrix A is stable. As a result, the combination of their ellipsoids via multiplication also remains positive-definite with a positive volume. The formulation of the metric is inspired by the Hankel operator Γ_G [10] defined below which has a similar formulation and provides a lower bound on the H_∞ norm of a system. The latter is utilized in robust control design, while the Hankel operator is used to define limitations in performing model reduction on larger complex systems to a simpler (fewer states)

system for control synthesis problems.

$$||\Gamma_G||_{L_2 \to L_2} = [\lambda_{max}(Y_o X_c)]^{\frac{1}{2}} \tag{2.18}$$

From Fig. 1.1, it is understood that the controllability gramian gives insight into the relative strength and weakness in controllability of the states, and similarly that the observability gramian gives insight into the relative strength and weakness in observability of the states of a system. However, there may indeed be a case as in Fig. 2.2 where the ellipsoid representations of the controllability and observability gramians are oppositely aligned. From an input-output perspective, the lesser observable states might still be impactful since they are the most controllable. As a result, better insight can be obtained from a balanced realization where both the X_c and Y_o are transformed by a similarity transformation T such that

$$\tilde{A} = TAT^{-1}, \tilde{B} = TB, \tilde{C} = CT^{-1}, \tag{2.19}$$

$$\tilde{X}_c = TX_cT^*, \tilde{Y}_o = (T^*)^{-1}Y_oT^{-1}. \tag{2.20}$$

From a balanced realization, it becomes evident that

$$\tilde{X}_c = \tilde{Y}_o = \Sigma, \tag{2.21}$$

with $\Sigma > 0$ diagonal, giving the insight that the less controllable states are also less observable. Further,

$$\tilde{Y}_o\tilde{X}_c = T^{-1}Y_oX_cT^*, \tag{2.22}$$

with the eigenvalues of $\tilde{Y}_o\tilde{X}_c$ and Y_oX_c coinciding. As a result, the square roots of the eigenvalues of Y_oX_C are called the Hankel singular values Γ_G of the system

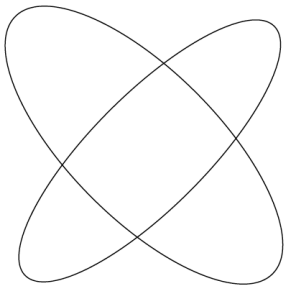

Figure 2.2: Oppositely aligned ellipsoid projections of controllability and observability gramians for a state-space system.

G and are denoted by $\sigma_1 \geq \sigma_2 \geq ... \geq \sigma_n$. The Hankel singular values provide upper and lower limits on the infinity norm of a realization of G ($\hat{G}$) in the following manner,

$$\sigma_1 = ||\Gamma_G|| \leq ||G|| = ||\hat{G}||_\infty, \tag{2.23}$$

and

$$||\hat{G}||_\infty \leq 2(\sigma_1 + \sigma_2 + ...\sigma_n). \tag{2.24}$$

The understanding of such a formulation using the observability and disturbance gramians in conjunction is that for a causal system, such an operation takes an input in the past and maps it to a future output. Therefore in the case that it is desirable to treat altitude gain as an energy metric, and vertical gusts are considered as the only disturbance inputs, the choice of C and D enable viewing the resultant M_G as a measure of perturb-ability in the vertical velocity state by a vertical gust. In particular, the volumetric size or determinant of this M_G is treated as numerically quantifying this notion. A gramian-aware control law would use a priori system

knowledge to derive a derive a mapping of M_G size as a function of one or several variables within its reach. From this map, the control law would react according to the following algorithm: a favorable gust (in this framework an updraft) would result in the controller driving the system towards those conditions where M_G size is maximum. Similarly vice-versa, in an unfavorable gust (downdraft), the controller would drive the system towards those conditions where M_G size is minimum in this a priori computed map. The idea is that such a gramian-aware controller, in comparison to a baseline controller that does not modulate the plant in response to a gust in either direction, will gain more altitude or energy in updraft sections, and lose less altitude in downdraft sections.

Chapter 3: Disturbance Sensitivity Modulation Through Parameter Sensitivity

3.1 Overview

From Equation (2.15), it is evident that cruise speed u_0 is an explicit term in the plant A matrix of the longitudinal LTI dynamics of a system. Moreover each of the stability derivative terms are cruise speed dependent as noted from Equations (3.1-3.3). It is evident that M_G as discussed in Chapter 2 is also a function of u_0 for any aircraft. In this chapter the Night Vapor BNF shown in Fig. 3.1 is considered for the modeling and experimental work.

Mass and size dimensions for the aircraft are included in Table 3.1. The inertia term of interest I_{yy} was calculated from a component-wise breakdown of the different parts of the aircraft that can be seen in Table 3.2. Each piece was individually weighed and measured to generate a Solid Works mockup from the component level. By setting the measured mass in the Mass Properties toolbox in Solid Works, the individual I_{yy} of each component was estimated. Note that in Table 3.2 and Fig. 3.2, the X and Z axes labels are not the body axes (which have in fact been labelled in Fig. 3.1). Instead, the axes have their origin at the lowest and

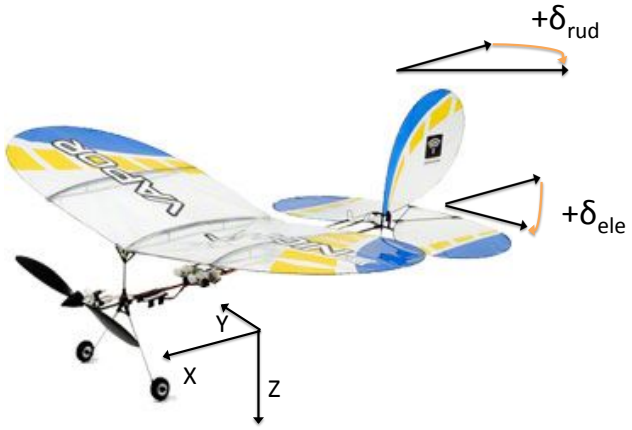

Figure 3.1: The Night Vapor BNF modeled and tested for this study.

most forward position on the aircraft to help determine the center of gravity location of the entire aircraft. The use of these axes is solely limited to the derivation of the aircraft CG and I_{yy}.

In the next section, the experimental system identification used to produce a mapping of the systems M_G size in terms of u_0 is discussed. Next, the system plant is modulated in Simulink using a gramian-aware controller.These results are compared against a baseline controller without modulation of u_0 in updrafts or downdrafts. Finally the experimental validation is presented via discussion of the gust generator rig and the results of the flight trials.

Parameter	Value
Mass m (kg)	0.0214
Wing Planform Area S (m^2)	242.05×10^{-4}
Chord Length $\bar{c}$ (m)	15×10^{-2}
Inertia I_{yy} $(kg * m^2)$	1303.969×10^{-7}

Table 3.1: Mass and size properties of the NightVapor BNF.

Piece	$m(g)$	Local $I_{yy}(g * cm^2)$	$X_{cg}(cm)$	$Z_{cg}(cm)$	Total $I_{yy}(g * cm^2)$
Fuselage	3.2	231.98	12.5	0.35	366.56
Prop	3.9	14.24	-1.95	1.3	265.90
Battery	4.6	6.23	2	-0.25	93.77
Servos	5	2.71	7.75	0.25	21.98
Wings	3.9	41.58	6.7018	5.1375	100.91
Elevator	0.6	3.31	29	0	319.42
Rudder	0.2	2.15	31.46	6.02	135.43
Total	21.4		6.08	1.29	1303.97

Table 3.2: I_{yy} calculation by component breakdown of the Night Vapor.

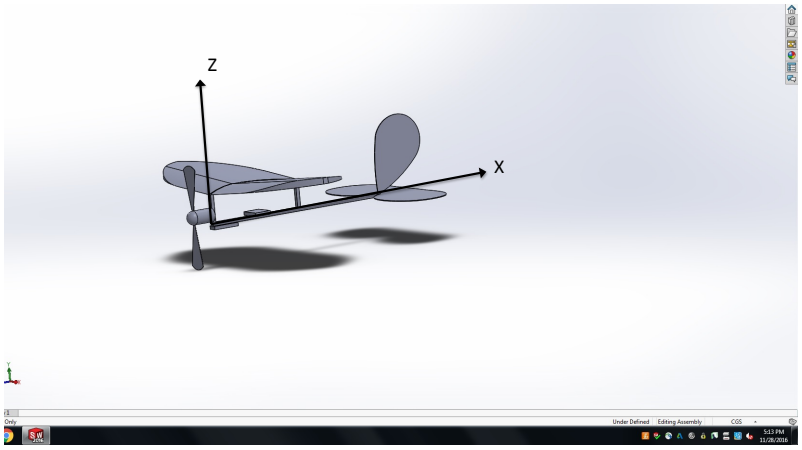

Figure 3.2: The Night Vapor BNF modeled in Solid Works by components for I_{yy} calculation.

3.2 System Identification

System identification was conducted via flight test in order to estimate the system's longitudinal plant characteristics at various cruise speed trim conditions. Using the following equations, the coefficients for the linearized longitudinal plant as well as the input-sensitivity were found

$$\dot{\Delta u} = \frac{C_{X_u} QS}{mu_0}\Delta u + \frac{C_{X_w} QS}{mu_0}\Delta w - gcos(\theta_0)\Delta\theta + X_{thr}\Delta_{thr}, \tag{3.1}$$

$$\dot{\Delta w} = \frac{C_{Z_u} QS}{mu_0}\Delta u + \frac{C_{Z_w} QS}{mu_0}\Delta w + u_0\Delta q + Z_{thr}\Delta_{thr} + Z_{ele}\Delta_{ele}, \tag{3.2}$$

$$\dot{\Delta q} = \frac{C_{m_u} QS\bar{c}}{I_{yy}u_0}\Delta u + \frac{C_{m_w} QS\bar{c}}{I_{yy}u_0}\Delta w + \frac{C_{m_q} QS\bar{c}^2}{2I_{yy}u_0}\Delta q + M_{thr}\Delta_{thr} + M_{ele}\Delta_{ele}, \tag{3.3}$$

where Q is the dynamic pressure taken as $\frac{1}{2}\rho u_0^2$, and the states (u, w, q, θ) refer to forward velocity, vertical velocity, pitch rate and pitch angle respectively. As

a result, the longitudinal plant A was constructed as a function of u_0 from the identified coefficients as

$$A = \begin{bmatrix} \frac{C_{X_u}QS}{mu_0} & \frac{C_{X_w}QS}{mu_0} & 0 & -g \\ \frac{C_{Z_u}QS}{mu_0} & \frac{C_{Z_w}QS}{mu_0} & u_0 & 0 \\ \frac{C_{m_u}QS\bar{c}}{I_{yy}u_0} & \frac{C_{m_w}QS\bar{c}}{I_{yy}u_0} & \frac{C_{m_q}QS\bar{c}^2}{2I_{yy}u_0} & 0 \\ 0 & 0 & 1 & 0 \end{bmatrix}. \tag{3.4}$$

The NightVapor BNF's longitudinal plant was identified and validated across different trials using a combination of elevator and throttle doublets and sinusoids of varying frequencies and amplitudes. A waypoint tracking method was employed to get the aircraft stabilized at a steady-state speed $u_0 \in [2, 3]m/s$ and straight-and-level. Then it was turned off while undergoing the stimulation input profile, and then turned back on to recover the aircraft. A brief discussion of the waypoint tracking autopilot method follows. For control purposes, a Vicon camera arrangement was used to observe the aircraft in real time via five markers placed upon its wing surface. The Vicon datastream was sent to a LabView module to evaluate all the current states such as position, translational and rotational velocities in absolute and local frames, etc. Based on these states, a simple PID-control loop was implemented within the same LabView program, which was then sent via a PCTx cable to the NightVapor BNF's transmitter as pulse-width-modulation (pwm) commands to the throttle, elevator and rudder servos. The entire execution loop time averaged between 45 and 60 milliseconds. The throttle command was regulated to a set cruise speed u_o value, with 0 pwm and 1000 pwm corresponding to motor-cutoff

and full-throttle respectively. A series of waypoints were set up for the vehicle to track within the Vicon-covered area as shown in Fig. 3.3. The desired flight path angle Γ_{des} to the upcoming waypoint, and current flight path angle Γ, were calculated from the current position and translational velocities. Then the elevator was commanded to meet this requirement, with 0 pwm and 1000 pwm corresponding to elevator trailing-edge up and down respectively by 20 degrees. Similarly, a desired heading angle Ψ_{des} to the upcoming waypoint, and current heading angle Ψ, were calculated and the rudder was commanded to meet this requirement, with 0 pwm and 1000 pwm corresponding to rudder trailing-edge right and left respectively by 30 degrees. Although the waypoint tracker was equipped to fly the Night Vapor around the room in repeatable manner until the battery expired, for this system identification effort, only one loop was run at a time using a fully charged battery such that available thrust would not be a variable in the trial data. Also, the waypoint tracker was tuned such that it could utilize the raw datastream from the Vicon software running at 300 Hz without any noise filtering on the position and velocity signals. However, for this system identification effort, single-pole low-pass filters were used to allow for proper data fitting, with time constant $\tau = 0.7$ on the translational velocity signals, $\tau = 0.85$ on the rotational velocity signals, and $\tau = 0.92$ on the acceleration signals. Ideally the longitudinal stimulation input for the trials would involve a chirp signal on the throttle or the elevator. However, due to the overall straightaway length limitation and distance required to stabilize the transients from launch, the trials with sinusoidal inputs only implemented a particular frequency on the control surface at a time. The range of frequencies swept overall

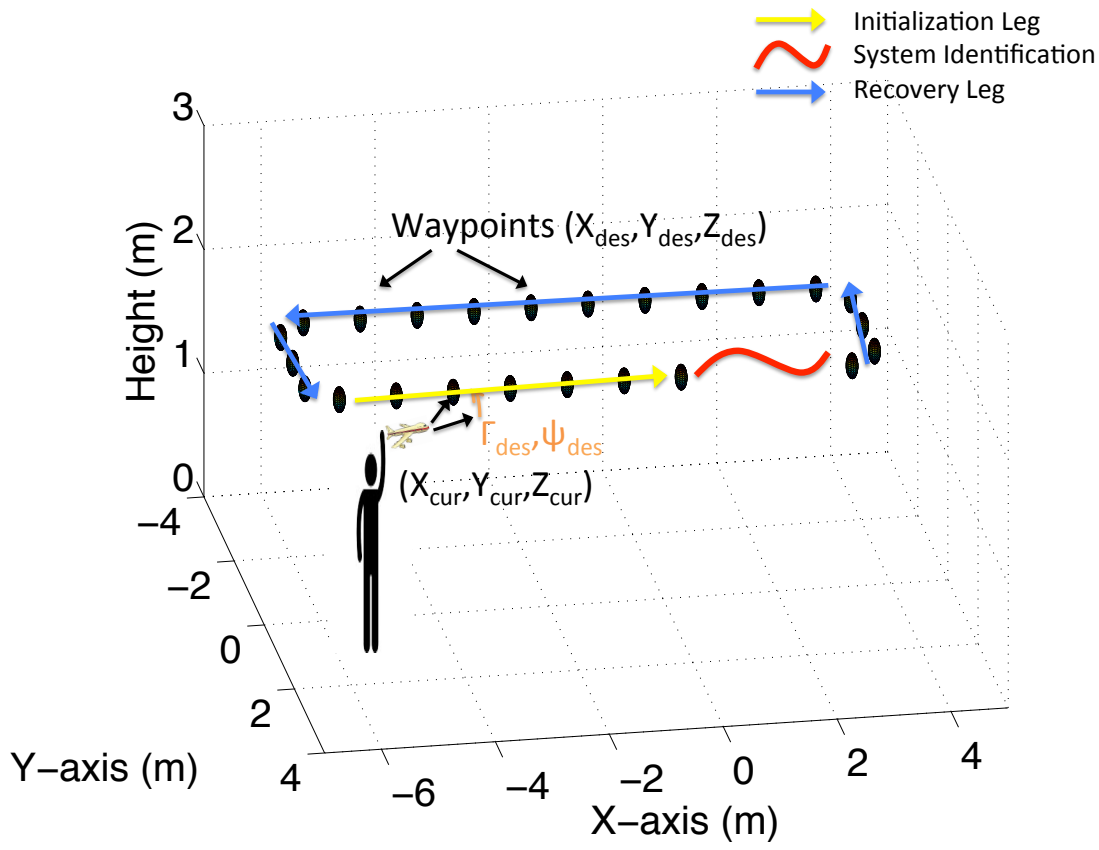

Figure 3.3: System identification conducted using waypoint tracker to stabilize aircraft a priori.

was $\in [0.006, 0.06] rad/sec$ and the amplitude modulation ranged from $\pm 300 pwm$ at the lower frequencies to $\pm 100 pwm$ at the higher.

Using the mass properties listed in Table 1 and taking $g = 9.81 m/s^2$ and $\rho = 1.225 kg/m^3$, the plant coefficients were estimated from Equations (3.1), (3.2) and (3.3) using an ordinary least-squares method [58] from the time-domain data. These coefficients have been listed in Table 3.3 along with their confidence intervals. The ordinary least-squares method is the solution to an overfitted problem by minimizing residual variance via appropriate selection of coefficients. Each of these coefficients

is provided as a nominal value along with a band in a Gaussian distribution about the nominal value, with the range up to 95% referred to as a confidence interval [59]. It was considered as a good fit on trial data if the width of this confidence interval was within 20% of the identified nominal value.

The coefficients were cross-checked from trials consisting of different control input profiles for repeatability. The identification trials and their repeatable counterparts for the coefficients derived from Equations (3.1-3.3) have been provided in Figures 3.4-3.6, respectively. Besides the check for repeatability and narrow confidence intervals, the coefficients were also validated across different control input profiles using autocorrelation analysis on the residuals. A number of different statistical metrics provide insight into the quality of the validation fit for a parameter by quantifying the whiteness of the residual autocorrelation. The Durbin-Watkinson statistic [60] was computed for this purpose for all seven validation exercises provided in Figures 3.7-3.13,

$$d_{stat} = \frac{\sum_{t=2}^{T}(e_t - e_{t-1})^2}{\sum_{t=1}^{T}(e_t)^2}, \tag{3.5}$$

where T is the total number of measurements and each e_i is a particular residual between the measurement and the estimate using the identified coefficient. The range for $d_{stat} \in (0, 4)$, with 2 indicating no autocorrelation in the residuals. Smaller values of this mean that consecutive residuals are close to one another, or in other words positive autocorrelation. In time-domain data, some positive autocorrelation is to be expected. For the purpose of this validation exercise, $d_{stat} < 0.95$ was taken as a benchmark for poor validation on a coefficient [61].

A related statistical measure is the autocorrelation itself, defined as

$$\hat{R}_{vv} = \frac{1}{T}\sum_{t=2}^{T} e_t e_{t-1}. \tag{3.6}$$

Here, $\hat{R}_{vv} = 0$ indicates no autocorrelation in the residuals and perfect randomness to them. Again, since such a result is never exactly attainable, [62] even for an adequate model structure, it is acceptable to have values near 0 as long as the zero autocorrelation is within ± 2 standard errors of the residual autocorrelation estimate [63]. The standard error is defined as

$$s(\hat{\theta}) = \sqrt{\frac{\sum_{t=1}^{T} e_t^2}{T - n_p}}, \tag{3.7}$$

where $n_p = n + 1$ and n is the number of unknown parameters in the validation exercise. These results are provided in the last two columns of Table 3.3. For all seven coefficients identified, with the autocorrelation in the residuals appearing near 0 in the sense that their standard errors are much larger, the residuals from the validation trials can be considered as white and not indicative of a statistical significance or model inadequacy.

Taking the coefficients listed in the first identified column in Table 3.3, the plant matrix A was constructed across the range of flight speeds appropriate for the NightVapor according to Equation (3.14). The migration of the open loop poles of the system identified model as a function of forward speed are shown in Fig. 3.7. As expected, the aircraft tends towards instability near the slower end of its speed range, and higher stability and damping of transients at the faster end of its speed range. Of more interest, is Fig. 3.15, illustrating the function of the disturbance

Parm	Val ID (1)	Conf Int (1)	Val ID (2)	Conf Int (2)	d_{stat}	$\hat{R}_{vv}$	$s(\hat{\theta})$
Eqn (3.1)							
C_{X_u}	-1.557	19.7%	-2.1142	19.8%	2.04	-0.0075	0.1968
C_{X_w}	3.2337	18.2%	3.0746	11.6%	1.15	0.0046	0.1390
Eqn (3.2)							
C_{Z_u}	-0.9241	15.9%	-1.2684	27.6%	1.70	0.0082	0.2800
C_{Z_w}	-5.1705	6.4%	-4.2455	17.8%	0.99	0.1249	0.5909
Eqn (3.3)							
C_{m_u}	0.0441	16.3%	0.0448	12.7%	1.55	0.0011	0.0740
C_{m_w}	-0.1079	3.2%	-0.1577	70.8%	1.10	0.1226	0.5880
C_{m_q}	-0.5556	17.6%	-0.4927	28.7%	1.35	0.0006	0.0954

Table 3.3: Longitudinal dynamics plant coefficients of the NightVapor BNF derived from experimental system identification across multiple trials.

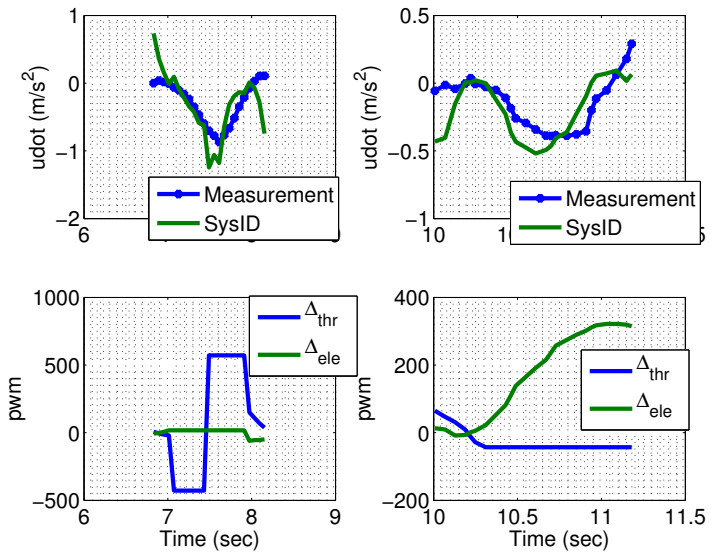

Figure 3.4: Identification and repeatability trials for Equation (3.1) plant parameters

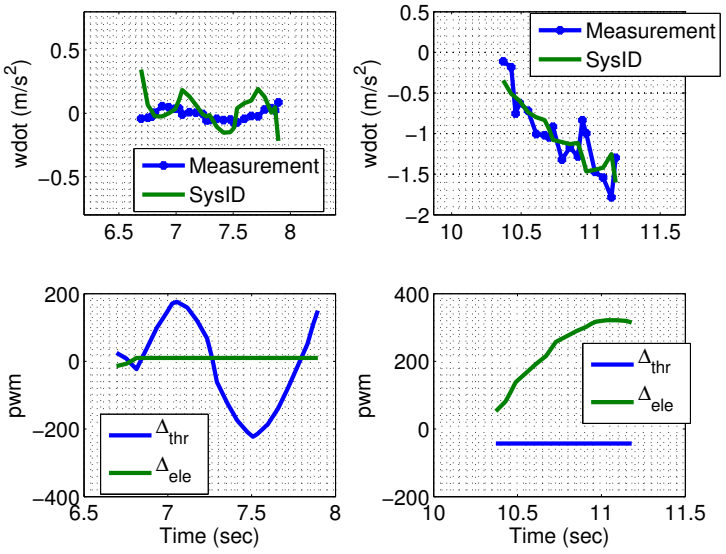

Figure 3.5: Identification and repeatability trials for Equation (3.2) plant parameters

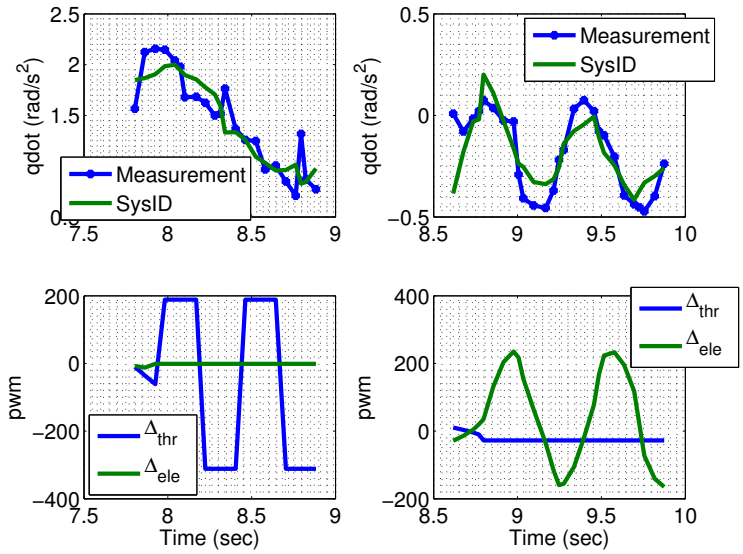

Figure 3.6: Identification and repeatability trials for Equation (3.3) plant parameters

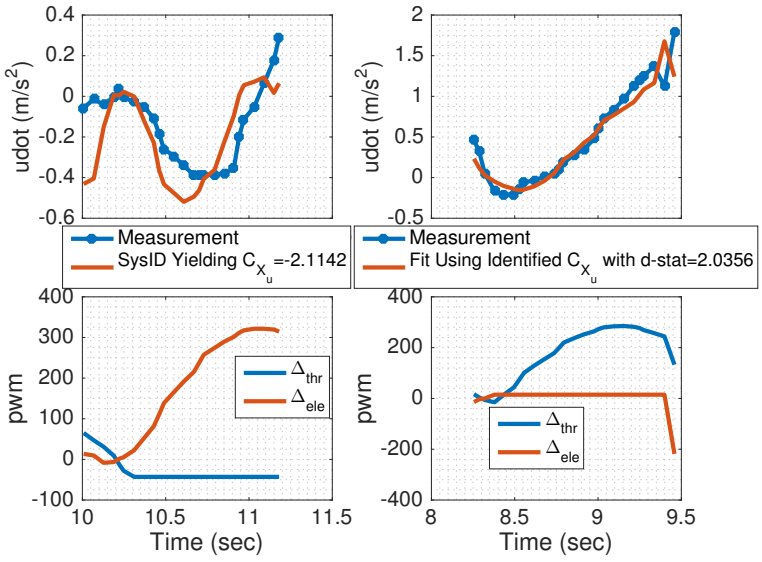

Figure 3.7: Validation of identified C_{X_u} value from a different trial

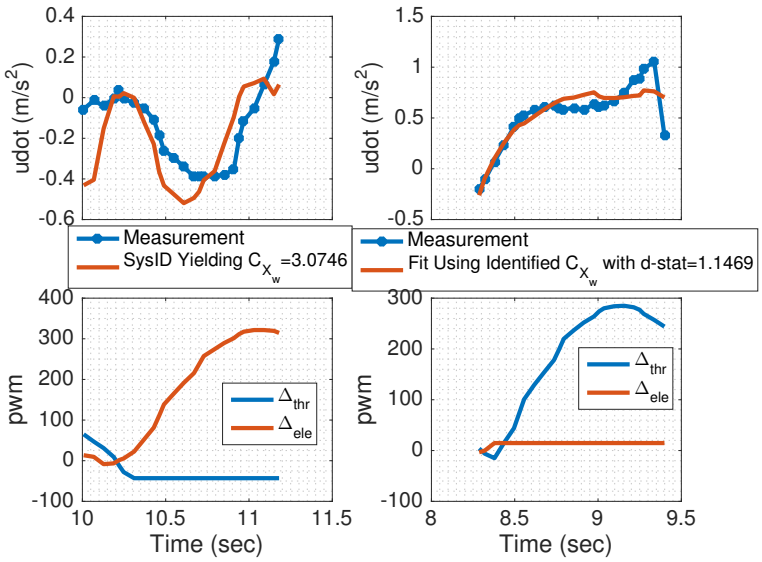

Figure 3.8: Validation of identified C_{X_w} value from a different trial

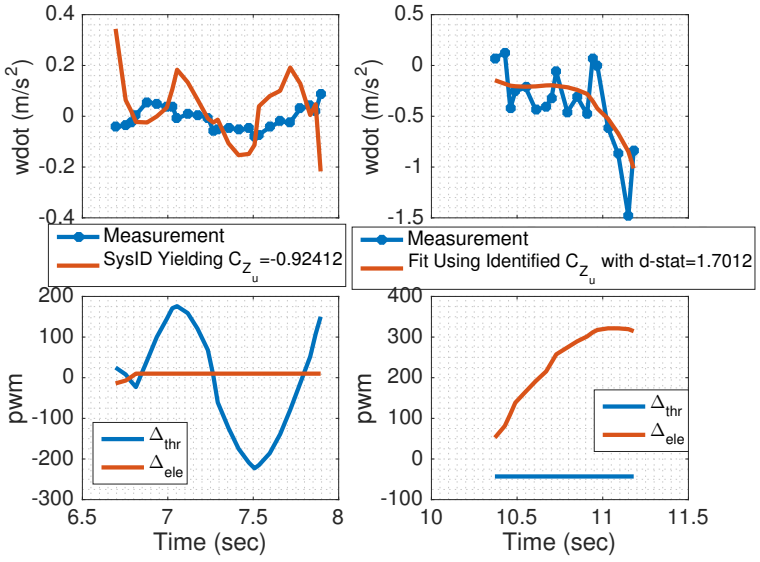

Figure 3.9: Validation of identified C_{Z_u} value from a different trial

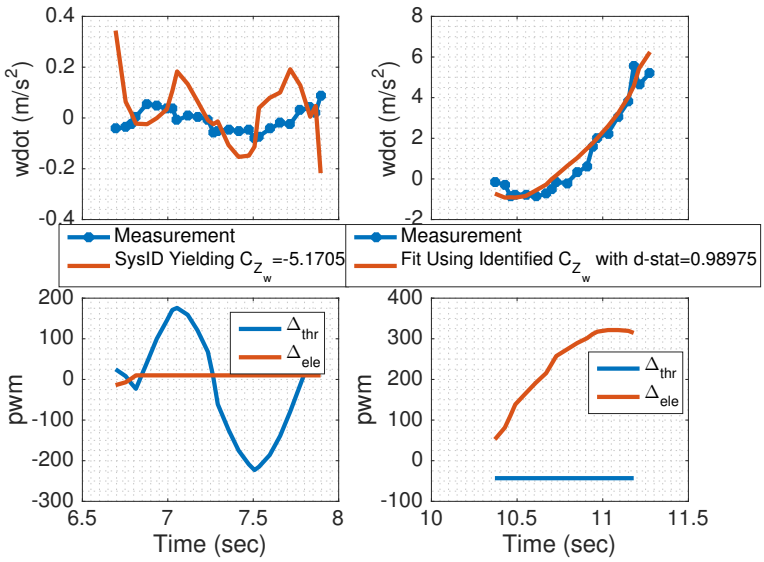

Figure 3.10: Validation of identified C_{Z_w} value from a different trial

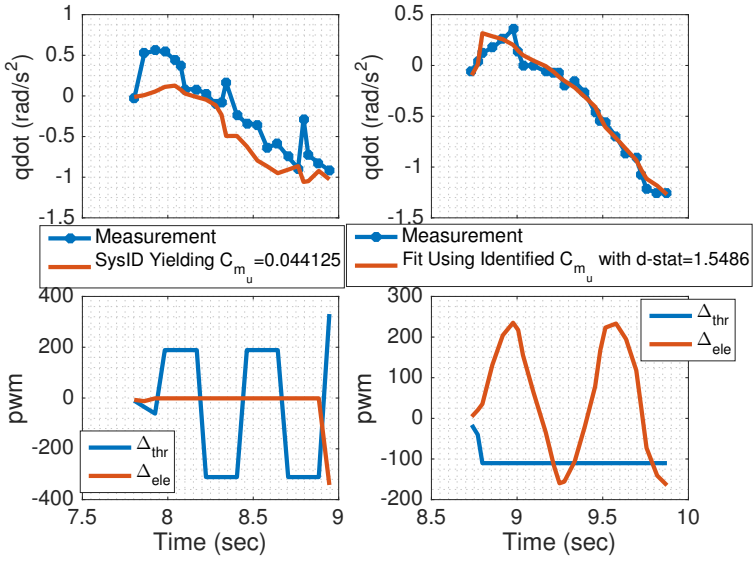

Figure 3.11: Validation of identified C_{m_u} value from a different trial

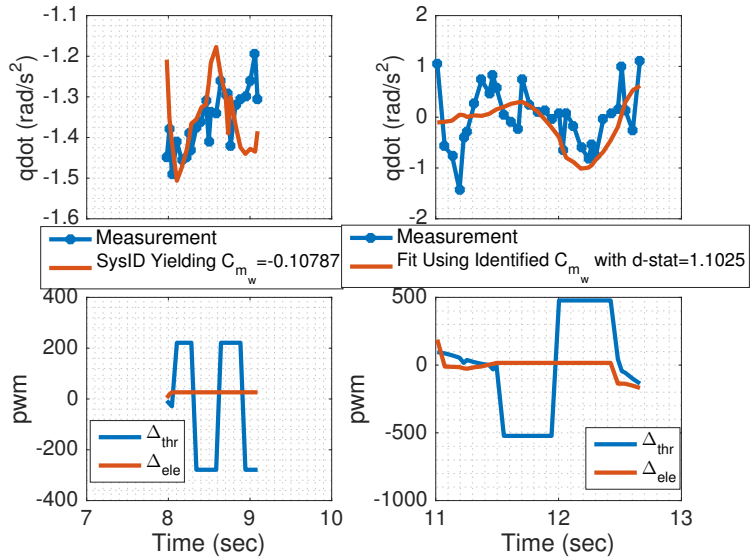

Figure 3.12: Validation of identified C_{m_w} value from a different trial

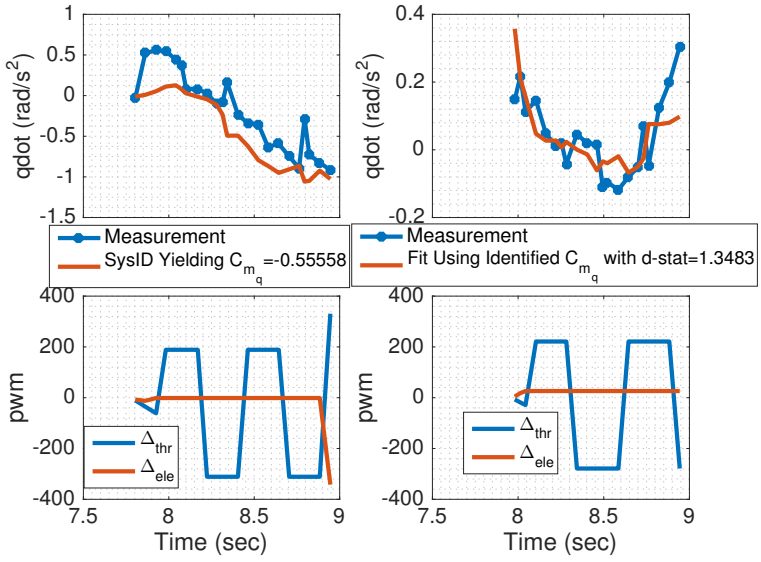

Figure 3.13: Validation of identified C_{m_q} value from a different trial

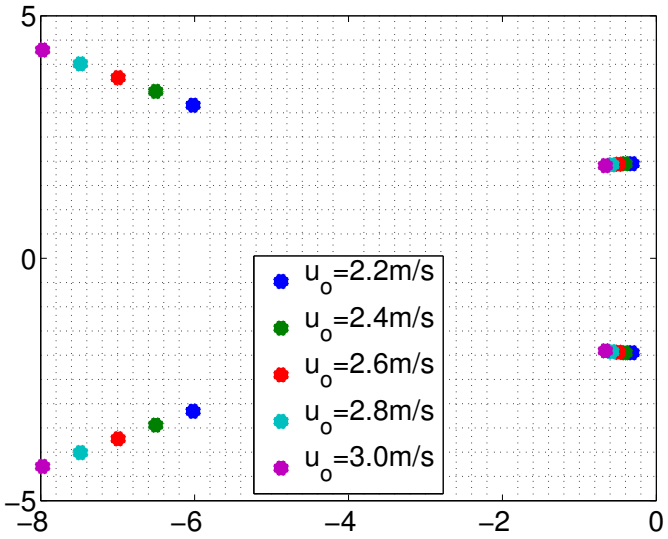

Figure 3.14: Open loop pole movement of system identified A matrix as a function of trim speed u_0.

and observability gramian ellipsoid volumes as a function of trim speed u_0 as well as that of the resultant M_G volume.

3.3 Cruise-speed Modulating Gramian-Aware Law Simulation

As mentioned in Chapter 2, the map in Fig. 3.15 is used to develop a gramian-aware cruise-speed modulating control algorithm for the Night Vapor in the following manner. In the absence of any gusts, the Night Vapor flies at an intermediate speed of $u_0 = 2.6m/s$. When it enters a region with a favorable gust (updraft) of $w_g = -1m/s$, it modulates itself to the speed that corresponds to the largest M_G size, which in this case will be $u_0 = 2.2m/s$. When it leaves the updraft section, it returns to its intermediate-M_G-size corresponding speed of 2.5m/s as it was flying

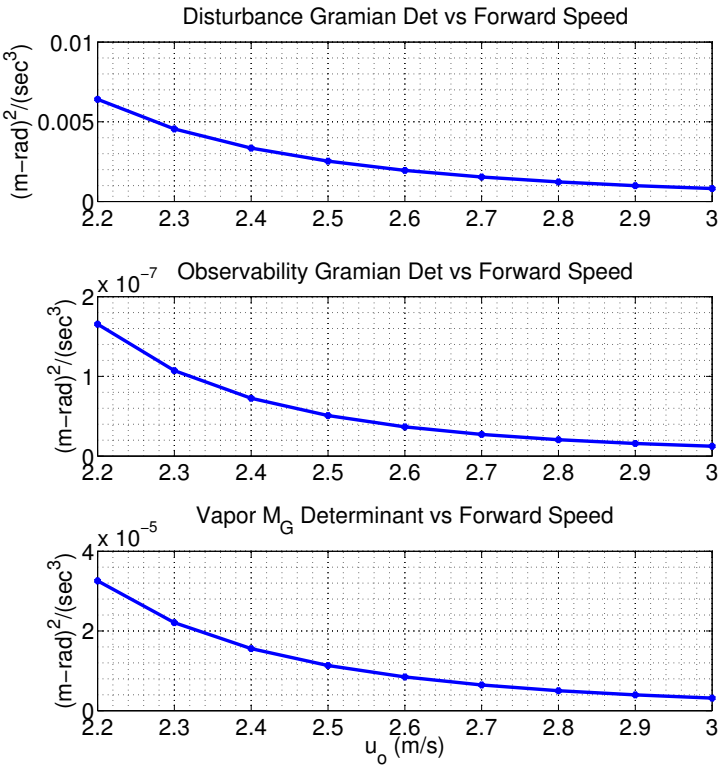

Figure 3.15: Disturbance gramian, observability gramian and gust capture metric volume as a function of trim speed.

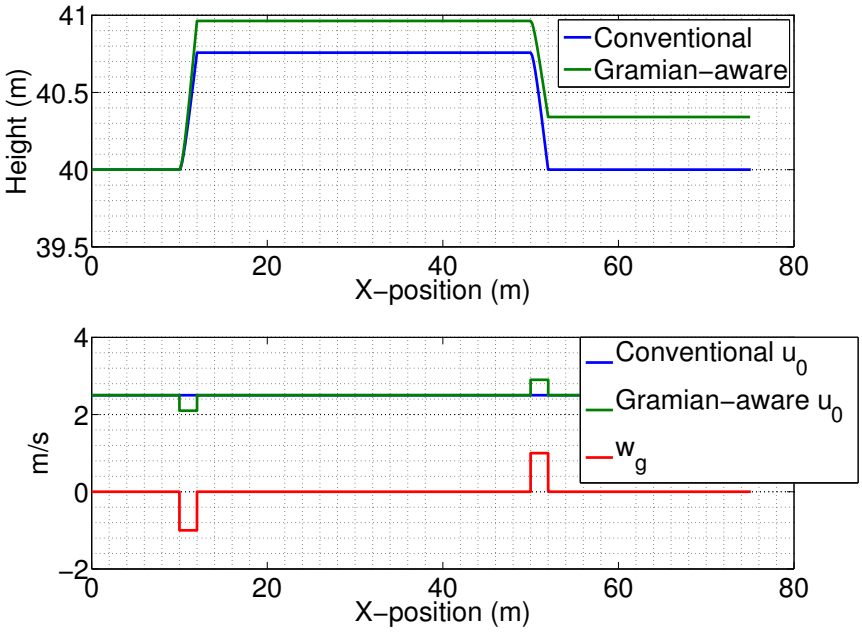

Figure 3.16: Simulation of the NightVapor BNF over a gust field of equal and opposite gust sections with gramian-aware and conventional control laws.

originally. Once the aircraft enters an unfavorable gust (downdraft) of $w_g = 1m/s$, it modulates itself to the speed that corresponds to the smallest M_G size, which is $u_0 = 3.0m/s$. The results from such a simulation in idealized gust-sections of equal lengths and opposite magnitudes is shown in Fig. 3.16. For comparison, the baseline or conventional controller does not modulate its speed in either updraft or downdraft, and flies through the entire length at constant $u_0 = 2.6m/s$.

Both the M_G map in Fig. 3.15 and the simulation result in Fig. 3.16 make intuitive sense in that obviously a faster flying Night Vapor would be less impacted by a vertical gust than a slower flying Night Vapor. This intuitive behavior is being captured in this gramian-derived theoretical framework. As a result, a gramian-aware controller that is built with directionality awareness will be capable of scavenging

atmospheric energy in updrafts by modulating itself to the condition with higher M_G size, which in this chapter means a slower u_0, and vice-versa. In practical terms, the gramian-aware Night Vapor spent more time in the updraft and less time in the downdraft, and hence resulted with a net altitude gain over the Night Vapor that did not change its speed in either sections.

As a prelude to discussing the experimental results in the next section, some of the logistical issues are noted here briefly. Ideally the results of Fig. 3.16 would be validated using a similar strategy of an updraft and downdraft section. This necessitates the testing to be conducted indoors such that more control is maintained over the ambient gust field on the aircraft. Testing indoors causes limitations, primarily with regard to available area for testing, as well as size and proportionally related flight speed of the aircraft; one of the primary reasons why the Night Vapor was chosen for this demonstration purpose. Due to space limitations of a total straightaway length of about 9m, verification can be conducted only with an updraft generator. Also in the simulation of Fig. 3.16, the aircraft enters the gust sections at $u_0 = 2.6m/s$ and in the case of the gramian-aware flight it slows itself down to $u_0 = 2.2m/s$ instantly over the gust section length. Again due to space limitation, such an idealized speed change over a small gust section length of less than 2m is not possible. Instead the aircraft would fly at steady-state at a particular u_0 within its range prior to entering the gust section, and comparisons will be made on the different altitude gains across trials as a function of the entry steady-state u_0. A profile similar to Fig. 3.17 is expected in simulation over just the idealized updraft section with $w_g = -1m/s$ for 2m length. This type of a decreasing altitude

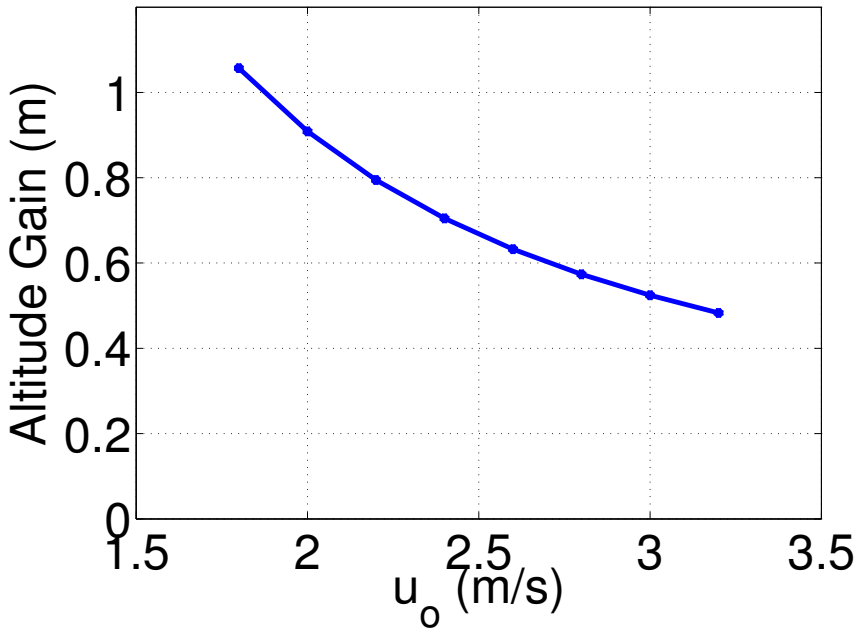

Figure 3.17: Altitude gain of a simulation of the system identified model over the speed range of the Vapor.

gain profile as a function of increasing cruise speed would equivalently validate the gramian-aware controller's effectiveness at atmospheric energy harvesting from an updraft.

3.4 Gust Generator

Flight tests were done using an upward gust generator. The gust generator, shown in Fig. 3.18 with dimensions, consisted of two B-Air 3550 CFM Air Mover's plugged in on opposite ends to a box with equally spaced holes along its top face. The box was 1.78m (70") long along the direction of flight (labeled as the X-axis), and 2.43m (96")wide (labeled as the Y-axis). The height of the box was 0.63m

(25"). Circular holes of 0.0508m (2") diameter were punched into the top face of the box in an evenly spaced manner such that there were 8 holes along the X-axis and 24 holes along the Y-axis in an evenly space and symmetric manner.

A velocity profile was measured by a uniaxial hotwire probe at two different heights of 1.52m (60") and 1.08m (42") from the top of the box. The measurements were taken in a spatial grid of every 0.3048m (12") across the box in the Y-direction and every 0.4572m (18") in the X-direction. Symmetry was assumed across the X-axis centerline of the box, resulting in a total of 33 measurements at each of the two heights aforementioned. Gust data was taken at 1000 Hz sampling rate for 20 seconds at each measurement location. An example measurement at $(X, Y, Height) = (0.9144, 1.2192, 2.15)m$ of the velocity versus time and the power spectral density have been shown in Fig. 3.19. The smooth contour of the power spectral density indicates that the turbulence generated in the gust generator was random and not contained in one particular frequency. Mean velocity contours are shown in Fig. 3.20, indicating an expected higher upward velocity over the center of the box as the air from the two blowers meet and rise.

A turbulence intensity for each measurement was defined as the root-mean square of the velocity fluctuation signal divided by the mean velocity [64]

$$Turb.Int. = \frac{\sqrt{\frac{1}{n}\sum_1^n (w_{g_i} - w_{g,0})^2}}{w_{g,0}}. \tag{3.8}$$

A turbulence intensity of 1% or less is generally considered low and turbulence intensities greater than 10% are considered high [65]. The average turbulence intensity across 33 measurement points at each altitude has been reported in Table

3.4. In Table 3.4 the average turbulence intensity over the middle half of the box at the two altitudes, i.e. from $Y \in [0.6096, 1.8288]m$ has also been noted. The RMS value on the signal has also been reported in a similar manner. Given that the mean does vary across the two altitudes as well as within each altitude spatially, and the fact that the turbulence intensity is normalized to the local mean while the RMS is not, both the normalized turbulence intensity and the RMS can give qualitative and quantitative insight into the flow characteristics in each of the regions.

Alt. Above Box (m)	Turb. Int. Whole	Turb. Int. Mid.	RMS (m/s) Whole	RMS Mid.
1.52	0.3323	0.2897	0.1742	0.1890
1.09	0.3632	0.3492	0.2253	0.2839

Table 3.4: Average turbulence intensities and root-mean-square of measured velocity at the two altitudes considered above the gust generator box.

3.5 Flight Test Results and Discussion

Flight tests using the waypoint tracker discussed earlier were conducted over the gust generator. The elevator control that tracked altitude was turned off for the flight portion over the gust generator section itself, such that the altitude gain from the gust could be evaluated without the bias of an elevator input attempting to attenuate the gust impact. Rudder and throttle control were active through the gust section in order to maintain flight over the center of the box and cruise speeds respectively. In order to effectively compare altitude gains across flight speeds, the controller was tuned to the effect that within the gust-generator region, the aircraft

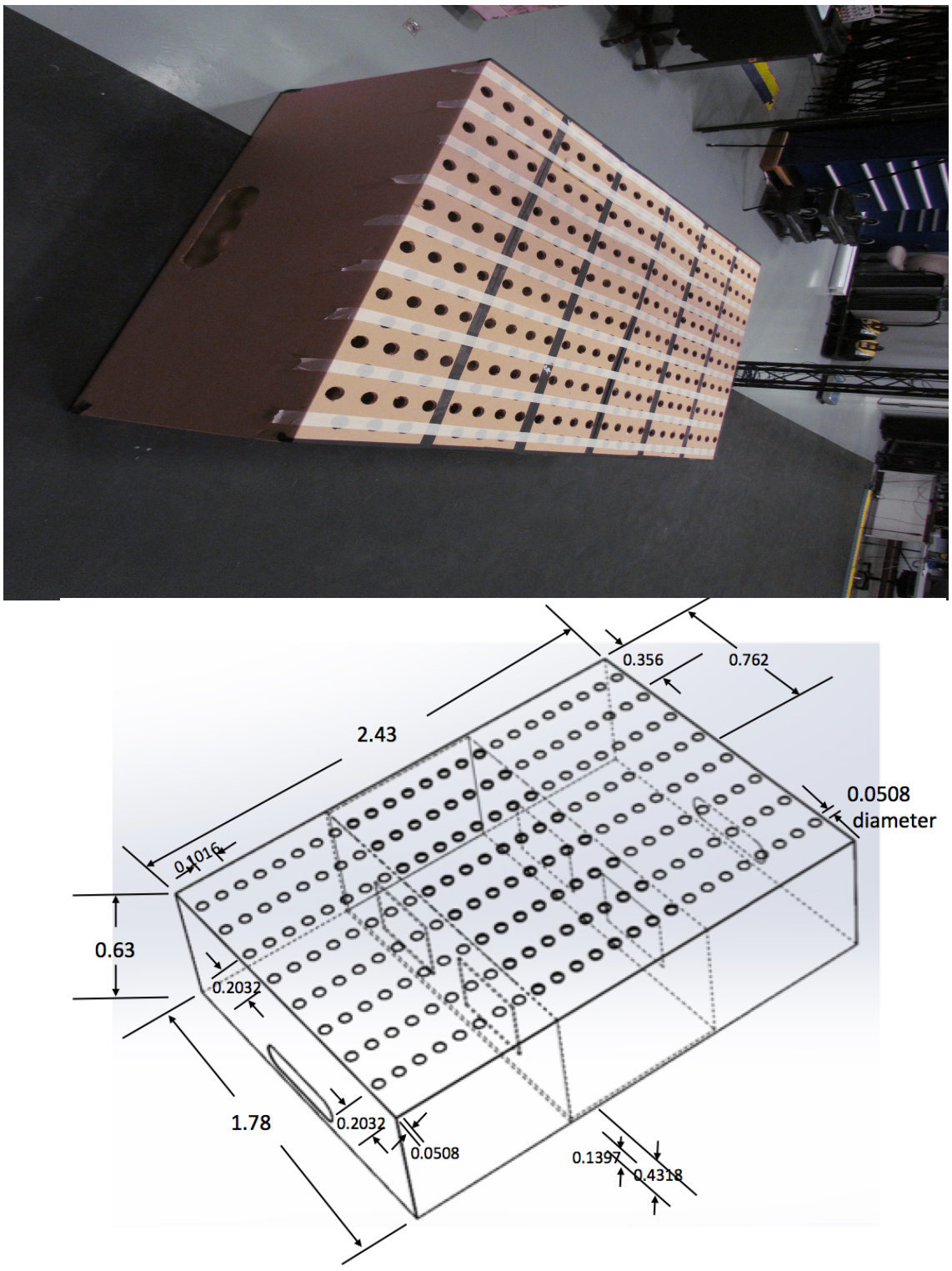

Figure 3.18: The gust-box generator used and corresponding dimensions in meters.

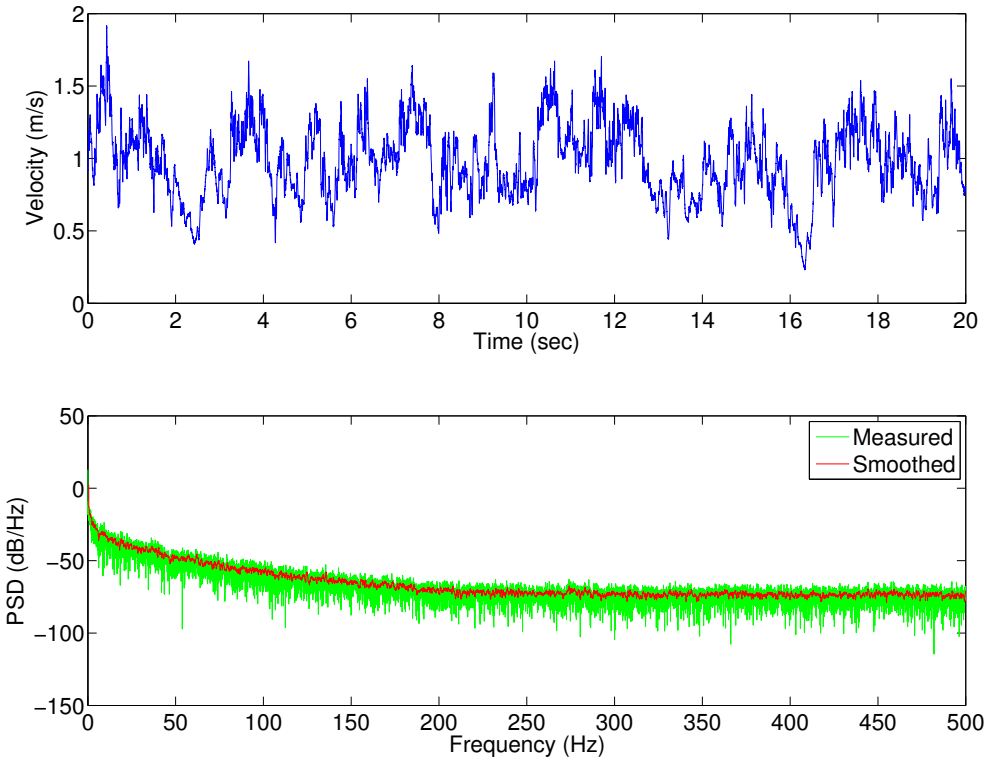

Figure 3.19: Measured velocity at 1.52m (60") above center of box and power spectral density of signal.

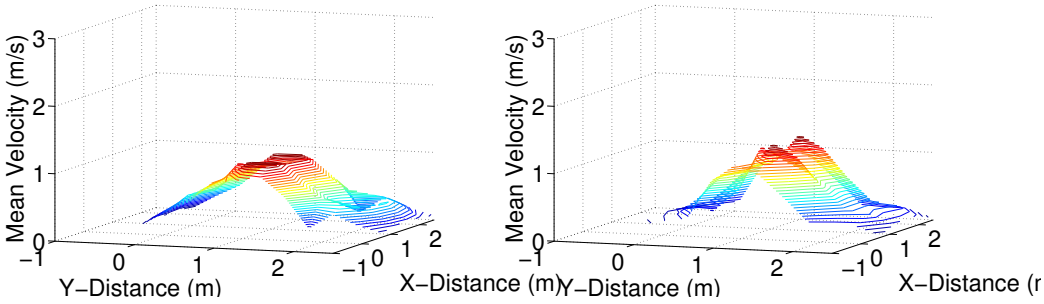

Figure 3.20: Mean velocities measured at 1.52m above box on the left, and 1.08m above box on the right.

would not gain or lose more than 0.1m of altitude while the gust was off. Such a "control" flight has been presented in Fig. 3.22, where the flight maintains minimal altitude change through the gust-section while the gust is off. An example flight over the gust-generator while on is shown in Fig. 3.23, where the gust generator starts at $x = 0m$ and ends at $x = 1.78m$, as has been shown in Fig. 3.21. The effective cruise speed is taken as the average u_0 from the last four measurements prior to entering the gust region, while the corresponding altitude gain is taken as the difference in altitude between when the aircraft leaves the gust region from when the aircraft entered the gust region.

Overall, there were 57 flights over the gust generator section that were deemed appropriate for consideration given that a steady-state straight-and-level flight was established prior to entry. Out of these 57 test points, a clear difference in trends could be seen if the points were separated into a higher entry height band of greater than 2.1m and a lower entry height band of less than the same. 31 test points lay in the entry height band of 2.1-2.3m, and their plot along with a linear fit and R^2 value of the fit have been presented in Fig. 3.24. The rest of the trials entered the gust section in a range of heights from 1.7-2.1m and their altitude gain summary as a function of cruise speed is shown in Fig. 3.25.

In lieu of Fig. 3.24, it is worthwhile to note that for gust-on trials that entered the gust zone at heights below 2.1m (generally 1.7-2.1m), the altitude gain had no such trends against entry speed as seen in Fig. 3.25, as evidenced by a much poorer R^2 value in the linear fit compared to that from Fig. 3.12. This can be explained from looking at Table 3.4. First note from Fig. 3.26 that all 57 of the

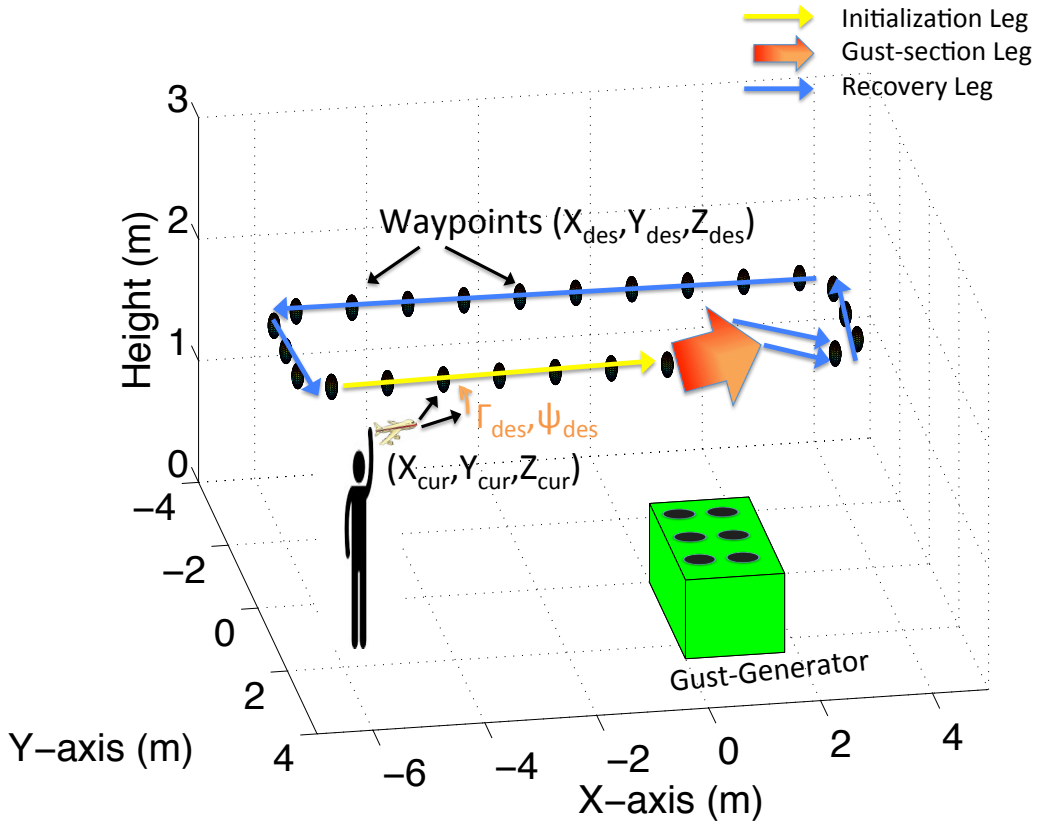

Figure 3.21: Flight trials to validate gramian-aware control conducted using waypoint tracker to stabilize aircraft a priori to gust generator.

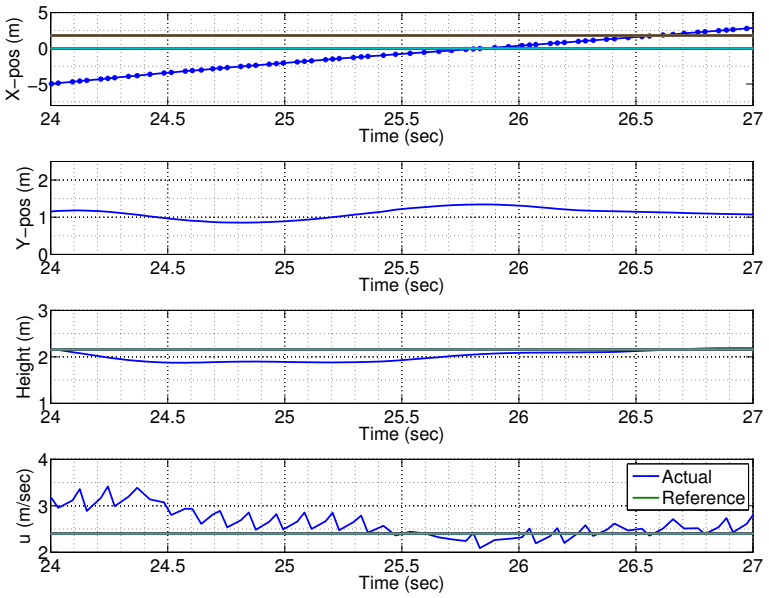

Figure 3.22: Example flight over gust generator with gust generator off used to tune controller to maintain altitude through gust section while gust is off.

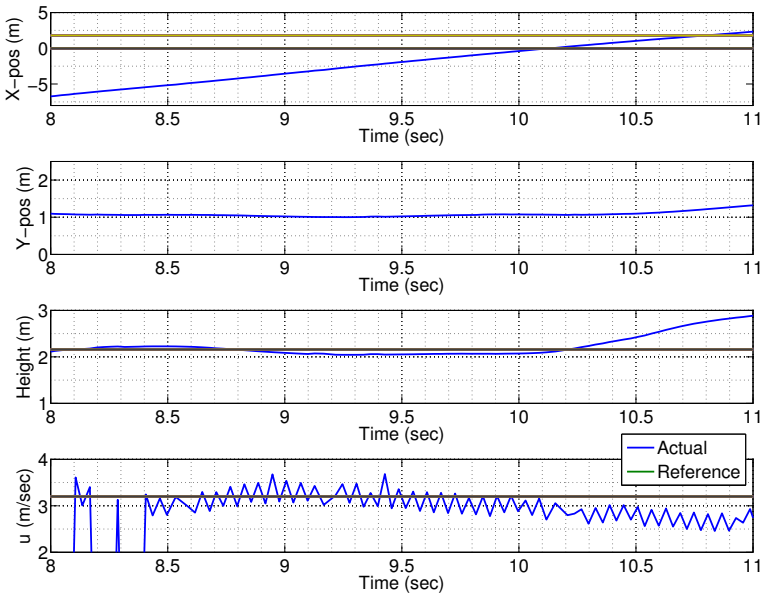

Figure 3.23: Example flight over gust generator with trim speed $u_0 = 2.94m/s$ and altitude gain of 0.685m.

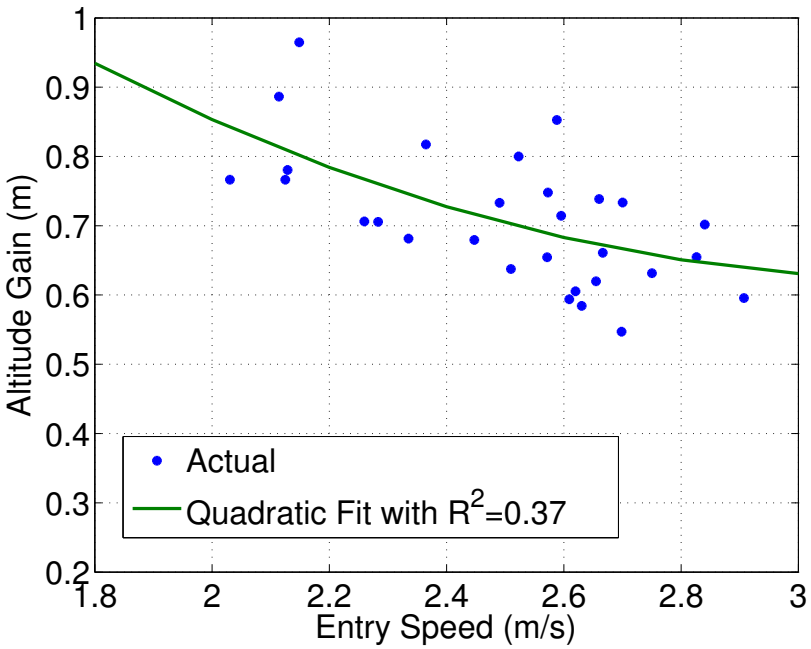

Figure 3.24: Summary of altitude gain vs entry cruise speed from flight test over the gust generator for entry altitudes above 2.1m and quadratic fit.

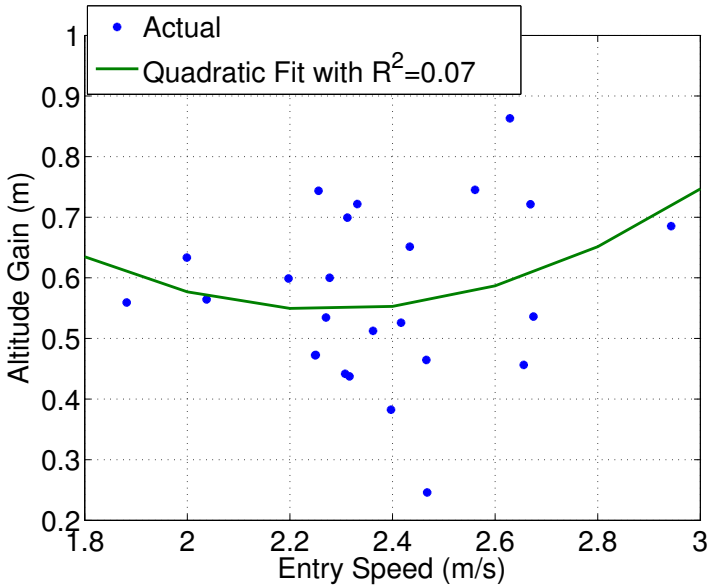

Figure 3.25: Summary of altitude gain vs entry cruise speed from flight test over the gust generator for entry altitudes below 2.1m and quadratic fit.

flights considered between Fig. 3.24 and Fig. 3.25 across the entire entry altitude range tended to fly over the middle half of the box, i.e. excluding the far-left and far-right quarters of the gust-generator box. Although the difference in the average turbulence intensity at the entry altitude above 2.15m taken across the whole gust box is 0.3323 as opposed to 0.3632 at 1.72m; if considering the middle half of the box $Y \in [0.6096, 1.8288]m$ over which all the flights flew, note that turbulence intensity at the higher altitude drops to 0.2897 while at the higher altitude it drops slightly to 0.3492. This significant difference in turbulence intensity as one goes higher in altitude above the gust-generator, particularly over the box's middle, allows for isolation of entry speed as the main factor in producing differences in altitude gains over the gust section. A similar trend can be noted in the non-normalized RMS value trends as well from Table 3.4. As a result, the experimental results of Fig. 3.24 validate the gramian-aware controller's energy harvesting effectiveness since the gust profile in the altitude band here is relatively less turbulent and more uniform.

3.6 Summary of Cruise Speed Modulation

In this chapter, the Night Vapor fixed-wing small UAV was considered as a platform to test the hypothesis regarding the use of M_G size to build a gramian-aware controller modulating cruise speed to scavenge atmospheric energy from vertical gusts. A system identification by experiment was utilized in order to build the map for M_G size as a function of u_0. A comparison by simulation was done where the gramian-aware Night Vapor would fly over updrafts at the u_0 that corre-

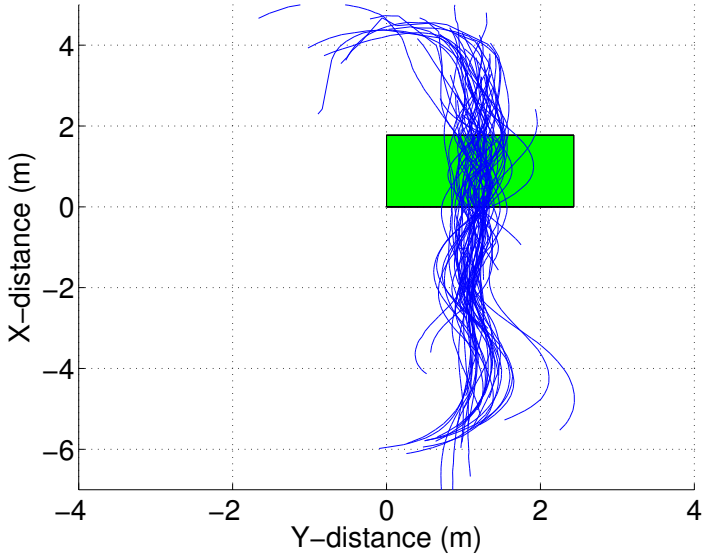

Figure 3.26: A look at trajectory profiles of gust-on flights across all entry altitudes and speeds.

sponded to its highest M_G size, and fly over downdrafts at the u_0 that corresponded to its lowest M_G size, as opposed to a gramian-blind or conventionally controlled Night Vapor which would maintain an intermediate u_0 through all gust sections. In simulation, the gramian-aware case gained significantly more altitude than the conventional case as a whole. In experimental validation given the test area limitations, this meant establishing a decreasing profile of altitude gain with increasing cruise speed over the updraft gust generator. Such a profile was not seen across the whole set of 57 data points but was seen over the higher entry height band. The gust characterization effort indicates that at this higher height of 5 feet above the top of the box and spatially over the middle half of the box, the aircraft trajectory is flying much closer to the ideal gust conditions considered in simulation than at the lower height of 3.5 feet above the box where the flow is much more turbulent. While im-

proving performance in turbulent gusting environments is indeed desirable, in terms of experimental validation, the data from the relatively less turbulent rising section above the middle of the box at the higher entry altitude is of more interest. As a result, the experimental results from the appropriate entry region indeed support the gramian-aware control law's premise for harvesting atmospheric energy better.

In Fig. 3.15, both the disturbance gramian and the observability gramians for the Night Vapor have an inversely proportional relationship with increasing cruise speed, and as a result the M_G has a similar profile. In [35], the longitudinal plant of the Apprentice UAV was modeled in DATCOM using four different airfoils. The disturbance, observability gramian ellipsoid and M_G volumes as a function of cruise speed for the Apprentice's speed range with NACA 66012 and NACA 2408 airfoils have been provided in Fig. 3.27. Instead of the M_G volume, if the disturbance gramian ellipsoid volume is chosen as the metric for the gramian-based speed modulation, the NACA 66012 model's disturbance-gramian-volume-based speed modulation has a net altitude gain over the constant-speed model while the NACA 2408 model's similar simulation has a net altitude loss over the constant-speed model as seen in Fig. 3.28 and Fig. 3.29. In the aforementioned figures, "Conventional" refers to the simulation that holds the speed constant over updrafts and downdrafts while "Gramian-aware" refers to the simulation where the respective Apprentice model modulates its speed according to the disturbance-gramian-ellipsoid-volume metric, i.e. maximize the disturbance gramian ellipsoid volume to an updraft and minimize it to a downdraft.

Defining a State Product Integrand S_P as the absolute product of the four

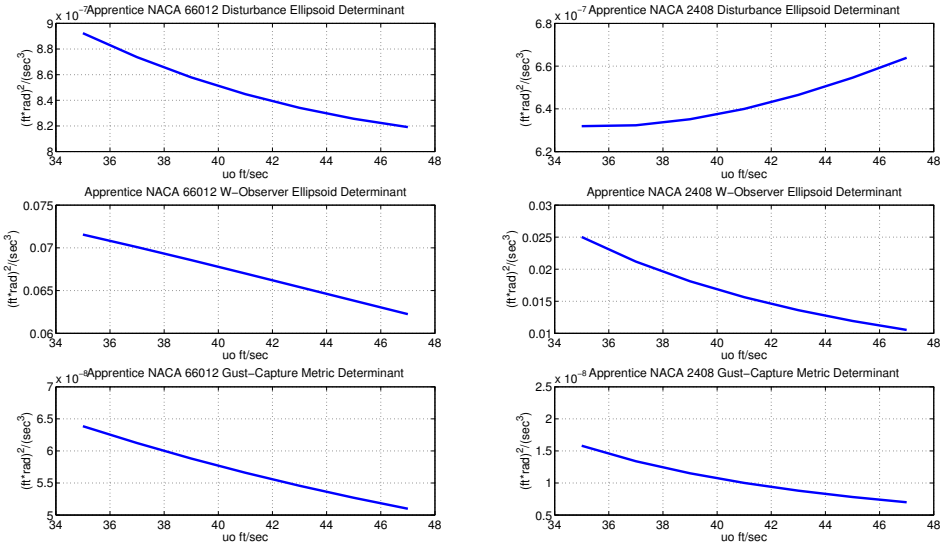

Figure 3.27: Apprentice UAV disturbance, observability gramian ellipsoid and M_G volumes as a function of u_0 for NACA 66012 and NACA 2408 airfoils.

states integrated over the simulation time over an updraft and downdraft for the disturbance-gramian-ellipsoid-volume-based speed modulation of Fig. 3.28 and Fig. 3.29

$$S_P = \int_{t_0=0s}^{t_f=50s} |\Delta u \Delta w \Delta q \Delta \theta| dt, \tag{3.9}$$

it is noted that the disturbance-gramian based modulation maximizes the S_P for both the NACA 66012 and NACA 2408 models as seen in Fig. 3.30 and Fig. 3.31. As a result, the disturbance-gramian-ellipsoid volume based speed modulation maximizes the total change in all the 4 states in updrafts and minimizes the same in downdrafts for both the airfoil models, as captured in the S_P metric. This exercise highlights the importance of involving the observability gramian as well in order to incorporate the desired direction, i.e. the vertical velocity state Δw along with the vertical gust such that the vertical gust's impact is maximized or minimized for up-

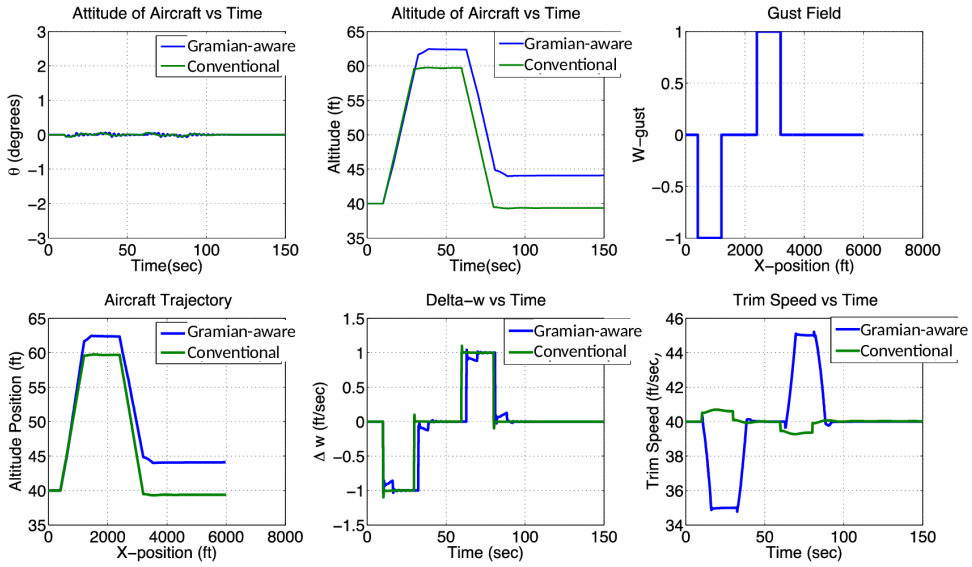

Figure 3.28: Apprentice NACA 66012 simulation over updraft and downdraft sections with speed modulation based on disturbance-gramian volume relation with u_0.

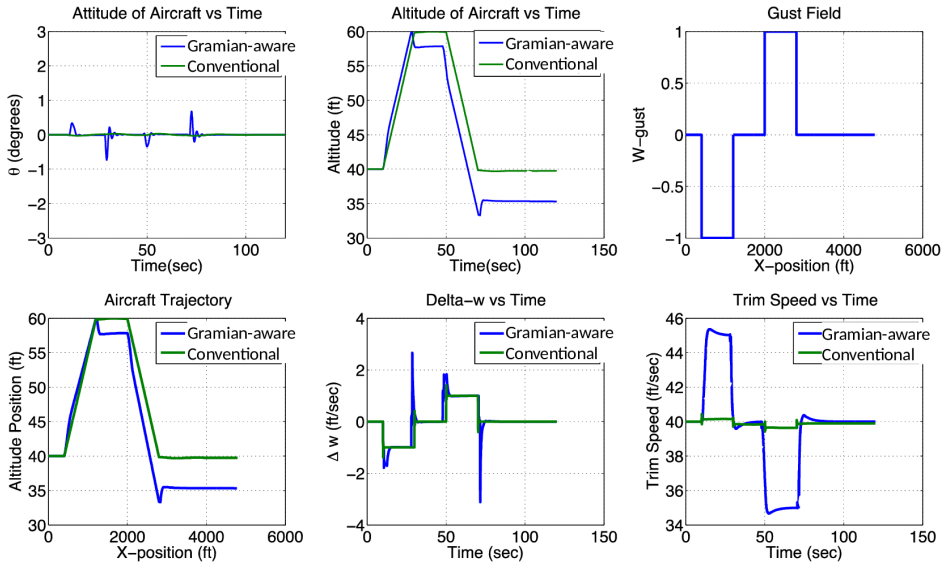

Figure 3.29: Apprentice NACA 2408 simulation over updraft and downdraft sections with speed modulation based on disturbance-gramian volume relation with u_0.

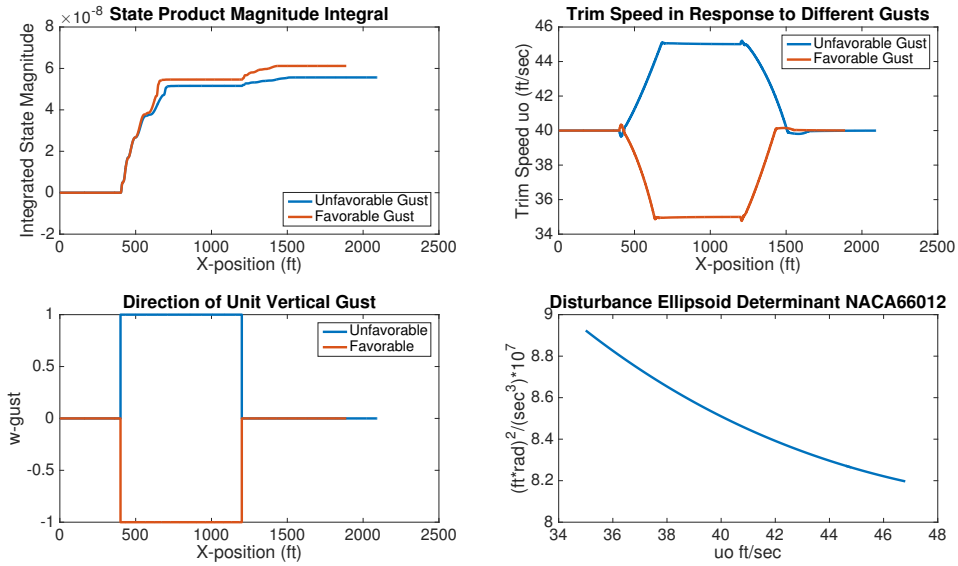

Figure 3.30: Apprentice NACA 66012 simulation of X_c based speed modulation maximizes S_P in updrafts and minimizes it in downdrafts.

drafts or downdrafts in the Δw direction in order to maximize altitude gain. Hence the M_G volume is taken as the basis for the gramian-based control since it incorporates both the overall disturb-ability in all states from a unit-norm vertical gust as well as the strength of observability of the desired state into a combined metric that quantifies the relative sensitivity in the Δw direction to a unit norm vertical gust. Simulating the Apprentice models according to the M_G volume variation as presented in Fig. 3.27, both the NACA 66012 and NACA 2408 models result in an altitude gain in simulation over the updraft and downdraft gust sections as seen in Fig. 3.32 and Fig. 3.33.

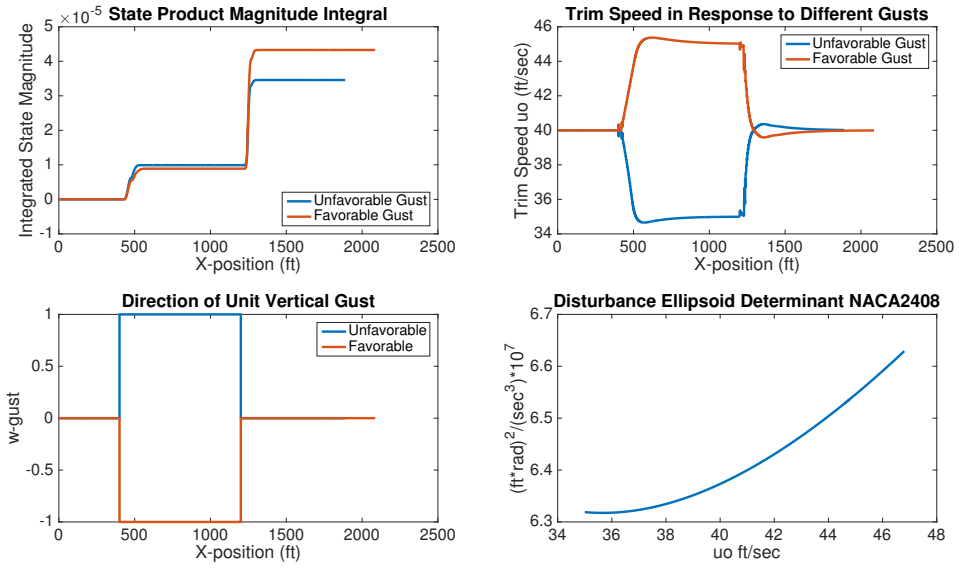

Figure 3.31: Apprentice NACA 2408 simulation of X_c based speed modulation maximizes S_P in updrafts and minimizes it in downdrafts.

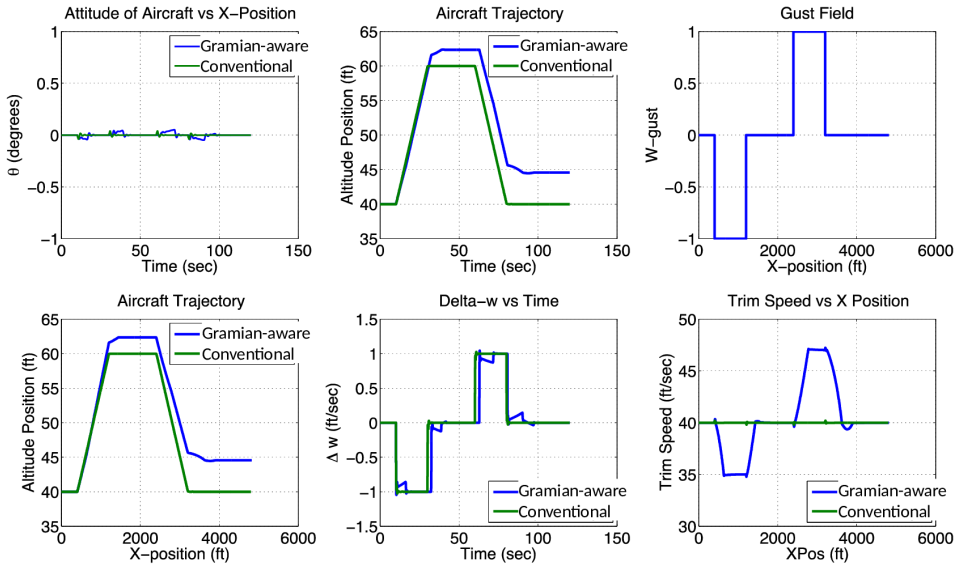

Figure 3.32: Apprentice NACA 66012 simulation over updraft and downdraft sections with speed modulation based on M_G volume relation with u_0.

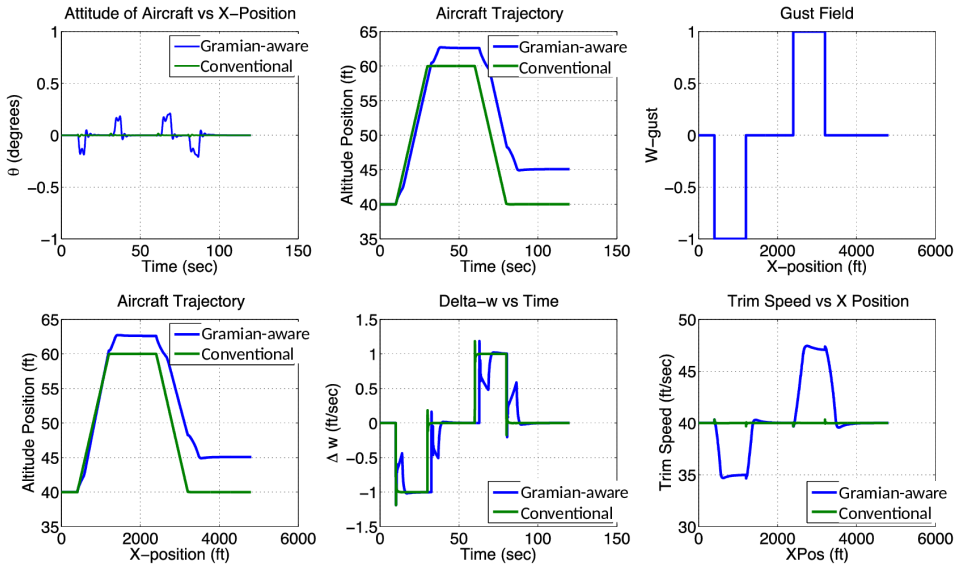

Figure 3.33: Apprentice NACA 2408 simulation over updraft and downdraft sections with speed modulation based on M_G volume relation with u_0.

Chapter 4: Disturbance Sensitivity Modulation Through Closed Loop Flight Control

4.1 Overview

A closed loop static gain controller was parametrized as $u = -Kx$, where traditional linear systems design techniques may be used to constructively design K. For illustration, the linear quadratic regulator (LQR) method was chosen to give a well-modeled design problem such that K can be posed as a function of weighting matrices, which has a well-understood intuitive meaning, rather than empirically considering various gains. In the LQR method [66], an optimal state feedback gain is computed based on minimizing the control input u given a user-defined penalization on deviations from the trim states in a positive-semi-definite Q matrix and a similarly defined penalization on deviations from the trim control input in a positive-definite R matrix. Note that the use of an LQR method is applied here as an example, but the gust response analysis approach developed here is not limited to a particular control design technique. Instead, it applies to general control design approaches that result in linear, static gain feedback.

Over a domain of varying (Q, R), the steady-state disturbance gramians of the

closed-loop system were calculated for a unit input vertical gust

$$(A - BK)X_c + X_c(A - BK)^* + DD^* = 0. \tag{4.1}$$

Also over the same space of (Q, R), the steady-state observability gramians of the closed-loop system were calculated for the vertical velocity state

$$(A - BK)^*Y_o + Y_o(A - BK) + C^*C = 0. \tag{4.2}$$

The size of the proposed M_G as a variation over the space of (Q, R) (and resultant controller gain K's) for each model was the basis for building a gramian-optimized control law. The determinants of the varying M_G's as a function of different closed-loop feedback controller gains is taken as having an implication on the vehicle's sensitivity in the vertical direction due to a vertical gust. A field with uniform lengths of equal and opposite magnitude unit vertical gusts was considered as the simulation environment, with gust lengths appropriately scaled for vehicle size and cruise speeds. The conventional controller would fly over both "favorable" and "unfavorable" gusts without changing its controller gains K, while the gramian-optimized controller would change its gains to that which corresponded to the largest M_G determinant (hereby labeled $\overline{M}_G$) for a "favorable" gust (updraft) and vice versa change its gains to that which corresponded to the smallest determinant (hereby labeled $\underline{M}_G$)to an "unfavorable" gust (downdraft).

Models were selected covering a range of scales for the longitudinal gramian analysis. The first two are of a small unmanned aircraft (Ultra Stick 25E) derived from DATCOM methods and flight-test-derived system identification respectively by

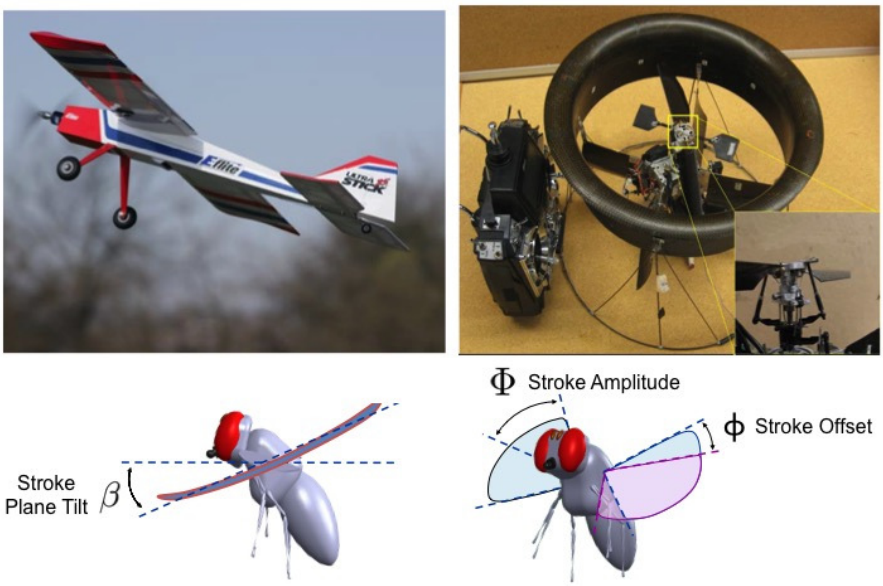

Figure 4.1: Ultra Stick 25E (top-left); Shrouded rotor MAV (top-right); Fruitfly (bottom).

Dorobantu et al., labeled (a) and (b) respectively. The differences in the two Ultra-Stick models, namely in the pitch damping M_q, make these models good candidates for exploring the sensitivity of our gust modeling approach to model origin [36]. The third model, labeled (c), is a decoupled hover model derived by system identification of a fruit fly *Drosophila* by Faruque et al. [**?**]. Next, the same fruitfly's full 3DOF dynamics model is considered, labeled (d). Finally, the shrouded rotor micro aerial vehicle derived via system identification by Hrishikeshavan et al. [68] is considered, labeled (e). Figure 4.1 shows the models considered here. Table 1 has the models enumerated and shows the several orders of magnitude considered in scale parameters.

Let the subscript notation refer to the system of interest. For example, $A_{(a)}$

System	Model	Mass m (kg)	Chord c (m)	Wingspan b (m)	I_y (kg m^2)
(a)	Ultra-stick (DATCOM)	1.959	0.25	1.27	0.144
(b)	Ultra-stick (Sys ID)	1.959	0.25	1.27	0.144
(c)	Fruitfly (Hover)	1.02×10^{-6}	1.3×10^{-3}	2.12×10^{-3}	5.96×10^{-10}
(d)	Fruitfly (Full 3DOF)	1.02×10^{-6}	1.3×10^{-3}	2.12×10^{-3}	5.96×10^{-10}
(e)	Shrouded Rotor MAV	0.257	N/A	0.244	N/A

Table 4.1: Parameters for the five systems.

indicates the open-loop plant matrix A for system (a). For systems (a), (b), (d) and (e), the x-axis is out the nose, y-axis out the right-wing and z-axis positive ventrally. The longitudinal state vector is

$$x = \begin{bmatrix} u & w & q & \theta \end{bmatrix}^T, \tag{4.3}$$

where u is surge, w is heave, q and θ are pitch rate and pitch angle respectively. The control input in (a) and (b) is an elevator deflection. For system (c), the control input is the flap amplitude Φ, while for system (d), the control inputs are the flap amplitude Φ, stroke plane angle β and mean position of wing oscillation ϕ. For system (e) the control inputs are the longitudinal cyclic and throttle. Control inputs for (d) and (e) were scaled to degrees and seconds (pwm), respectively. The gust vector g is

$$g = \begin{bmatrix} u_g & w_g & q_g \end{bmatrix}^T, \tag{4.4}$$

where u_g, w_g and q_g represent surge, heave, and rotational gusts. The longitudinal

gust-response matrix is taken as the negative of the plant dynamics matrix without the direct impact on the pitch angle state [12], thus resulting in the fourth row of the disturbance feedthrough matrix, D, being all zero. The vertical gust is considered by using the second column of D.

For the LQR methods discussed previously, $Q_{(a)}$, $Q_{(b)}$, $Q_{(d)}$ and $Q_{(e)}$ were of the form

$$Q_{(a,b,d,e)} = \texttt{diag}\begin{bmatrix} Q_u, & Q_w, & Q_q, & Q_\theta \end{bmatrix}, \tag{4.5}$$

while $Q_{(c)}$=Q_w, where Q_u, Q_w, Q_q and Q_θ refer to the individual weighting components for the respective states in the Q matrix. Similarly the R matrices for the systems were of the form

$$R_{(a,b,c)} = R_{11}, \tag{4.6}$$

$$R_{(d)} = \texttt{diag}\begin{bmatrix} R_{11}, & R_{22}, & R_{33} \end{bmatrix}, \tag{4.7}$$

and

$$R_{(e)} = \texttt{diag}\begin{bmatrix} R_{11}, & R_{22} \end{bmatrix}, \tag{4.8}$$

where R_{11}, R_{22} and R_{33} refer to the individual weighting components for the respective control inputs in the system under consideration. The vertical velocity observer for systems (a), (b), (d) and (e) was of the form

$$C_{(a)} = C_{(b)} = C_{(d)} = C_{(e)} = \begin{bmatrix} 0 & f & 0 & 0 \end{bmatrix} \tag{4.9}$$

while for system (c), $C_{(c)} = f$, where $f = \frac{|B_{()} B_{()}^T|_\infty}{(mb^2)^2}$ with $B_{()}$ referring to the relevant control input-output matrix and m and b taken from Table 1 as the mass and wingspan of the systems. The domain of (Q, R) over which controller gains and subsequent M_G volumes were calculated are the following: $Q_u \in [1, 20]$, Q_w, Q_q and $Q_\theta \in [1, 10]$; for systems (a), (b) and (c) $R_{11} = 1$; for (d) $R_{11} = R_{22} = R_{33} = 1$; for (e) $R_{11} = 1$, $R_{22} \in [1, 11]$.

4.2 Results and Discussion

The method identified a map for the M_G's determinant as a function of the varying Q's and R's [67]. Within the set, the maximum determinant $\overline{M}_G$ was identified with its corresponding $\overline{Q}$, the minimum determinant $\underline{M}_G$ was identified with its corresponding $\underline{Q}$. An intermediate $\tilde{M}_G$ determinant was chosen as the average of the largest and the smallest determinants in the set. If the search-space did not contain a (Q, R) that yielded a determinant close to the average of the largest and smallest determinants, then the second-highest or second-lowest M_G determinant was chosen as $\tilde{M}_G$. The corresponding Q was identified as $\tilde{Q}$. The conventional controller was simulated as a median set of gains corresponding to the $\tilde{Q}$. The gramian-optimized controller was gain scheduled such that it picked the gain from $\tilde{Q}$ when the vertical gust was zero, picked $\underline{Q}$ when the vertical gust was a downdraft, and picked $\overline{Q}$ when presented with an updraft. As a result of such gain scheduling, the presented method picks the gain that minimizes the impact of an unfavorable gust on the system's energy (altitude) and maximizes the impact of a

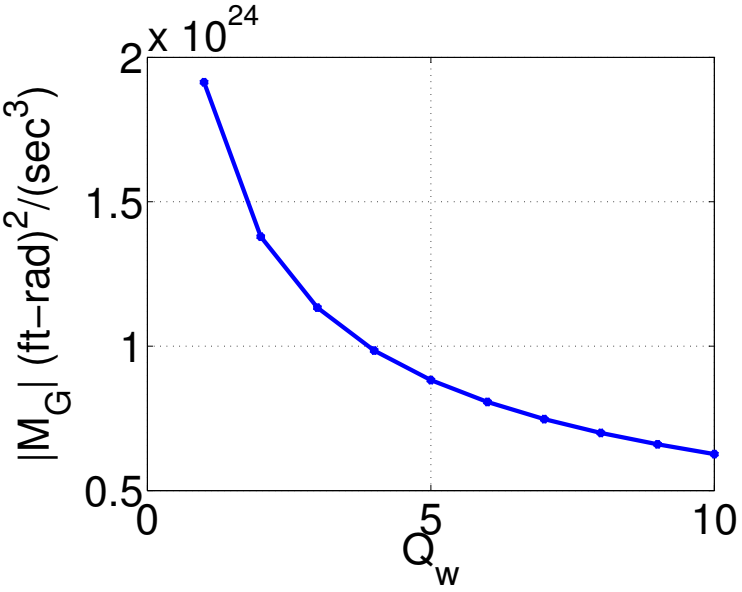

Figure 4.2: The determinant of M_G as a function of Q_w for system (c).

favorable gust.

Consider the uniaxial hover dynamics of system (c). As seen in Fig. 4.2, over the varying Q_w's, there is a variation in the determinants of the gust capture metric M_G.

From Fig. 4.2, there is a Q_w that corresponds to the highest M_G determinant in the set, as well as the lowest. These are thus labeled as $\overline{Q}$ and $\underline{Q}$, in this case being 1 and 10 respectively. The LQR gain K corresponding to these Q's are thus referred to as $\overline{K}$ and $\underline{K}$. For this case, $\overline{K}$ is -0.7564 and $\underline{K}$ is -2.8921. Finally, a $\tilde{Q}$ of 3 can be identified from the results in Fig. 4.2 as having the M_G determinant closest to the average of the maximum and minimum determinants and this corresponds to a $\tilde{K} = -1.4722$.

Figure 4.3 illustrates a simulation of the *Drosophila* in system (c) traveling at a constant forward speed of 0.4 m/sec through a gust field. There is a uniform

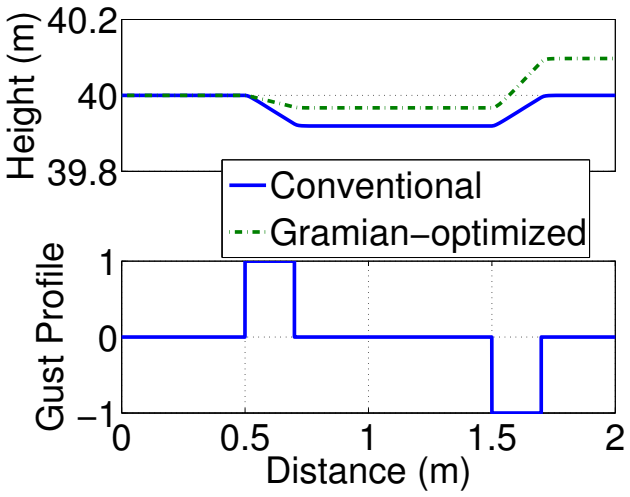

Figure 4.3: System (c) simulation indicates that gramian-gain switching allows altitude gain over conventional control.

downdraft section from 0.5 to 0.7 m, and then an equal and opposite updraft section from 1.5 to 1.7 m. The conventional controller flies through the entire track with constant gain $\tilde{K} = -1.4722$. The gramian-optimized case flies with the same $\tilde{K}$ when the vertical gust is zero. It is programmed to modulate its gain to $\underline{K} = -2.8921$ in the downdraft (unfavorable) section, returns to $\tilde{K}$ in the neutral gust section, and regulates its gain to $\overline{K} = -0.7564$ in the updraft (favorable) section. These results indicate a net improvement of the gramian-optimized K-regulator in comparison to the gramian-blind constant-K *Drosophila* model as the gramian-optimized case is able to minimize its altitude loss in the downdraft and maximize its altitude gain in the updraft. In totality, the gramian-optimized controller was able to harness more energy in the form of altitude gained from the flight over the updraft and downdraft sections in comparison to the gramian-blind fixed-gain controller.

Now consider the multivariate (Q, R) of systems (a), (b), (d) and (e). Over

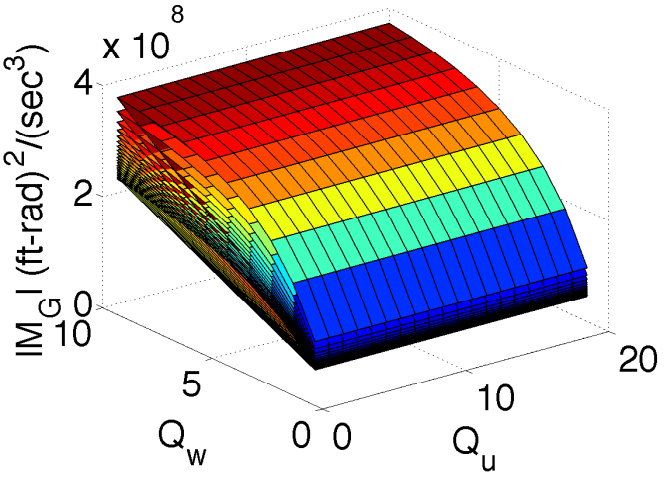

Figure 4.4: Bivariate projection of the Gust Capture Metric Determinant over Q_u and Q_w for System (b) while $Q_q = Q_\theta = 1$.

the ranges of Q_u, Q_w, Q_q and Q_θ's as shown in Table 2, we get an array of (Q, R) that correspond to maximum, minimum and a midpoint determinant of the gust capture metric M_G. The maximum, minimum and midpoint M_G determinants and their corresponding (Q, R) are noted in Table 2. A projection ellipsoid of the multidimensional M_G mapping for system (b) is provided below, keeping $Q_q = 1$ and $Q_\theta = 1$ in Fig. 4.4.

Subjecting systems (a), (b), (d) and (e) to a similar gust field, the results can be seen in Figures 4.5 through 4.8, each of which indicates the gramian-optimized controller gains more energy in the form of altitude gain over the conventional controller, as predicted theoretically. Since M_G is formulated primarily from knowledge of the system's plant and gust sensitivity dynamics, the optimal gains for a feedback loop in terms of atmospheric energy harvesting can be calculated off-board using this gramian-based maximizing and minimizing approach.

Parameter	(a)	(b)	(d)	(e)
Maximum				
$\overline{M}_G$	4.3162×10^{7}	3.7173×10^{8}	4.8192×10^{2}	9.324×10^{-1}
$\overline{Q}_u$	1	1	2	13
$\overline{Q}_w$	8	10	5	1
$\overline{Q}_q$	1	1	7	5
$\overline{Q}_\theta$	1	1	5	8
$\overline{R}_{11}$	1	1	1	1
$\overline{R}_{22}$	N/A	N/A	1	11
$\overline{R}_{33}$	N/A	N/A	1	N/A
Minimum				
$\underline{M}_G$	5.8109×10^{4}	1.6124×10^{5}	0	0
$\underline{Q}_u$	20	20	1	13
$\underline{Q}_w$	1	1	10	10
$\underline{Q}_q$	10	10	1	1
$\underline{Q}_\theta$	10	10	3	1
$\underline{R}_{11}$	1	1	1	1
$\underline{R}_{22}$	N/A	N/A	1	1
$\underline{R}_{33}$	N/A	N/A	1	N/A

Table 4.2: Identified (Q, R) values that correspond to maximum and minimum M_G determinants.

Parameter	(a)	(b)	(d)	(e)
Intermediate				
$\tilde{M}_G$	2.1610×10^{7}	1.8594×10^{8}	1.549×10^{-1}	4.662×10^{-1}
$\tilde{Q}_u$	11	13	18	12
$\tilde{Q}_w$	3	5	5	1
$\tilde{Q}_q$	1	1	6	3
$\tilde{Q}_\theta$	2	3	8	9
$\tilde{R}_{11}$	1	1	1	1
$\tilde{R}_{22}$	N/A	N/A	1	11
$\tilde{R}_{33}$	N/A	N/A	1	N/A

Table 4.3: Identified (Q, R) values that correspond to intermediate M_G determinants.

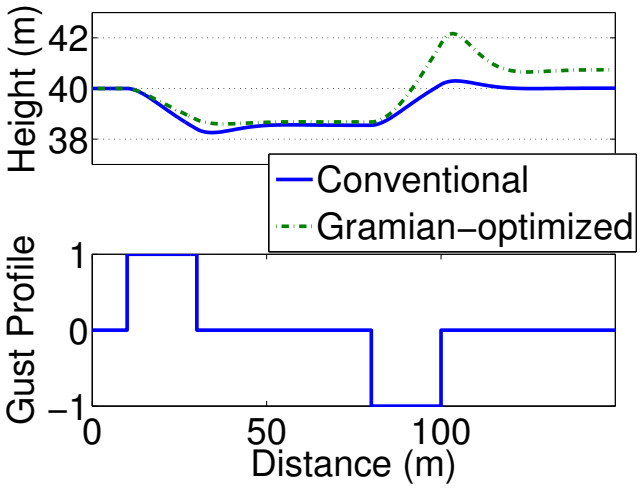

Figure 4.5: Flight trajectory over gust field for system (a).

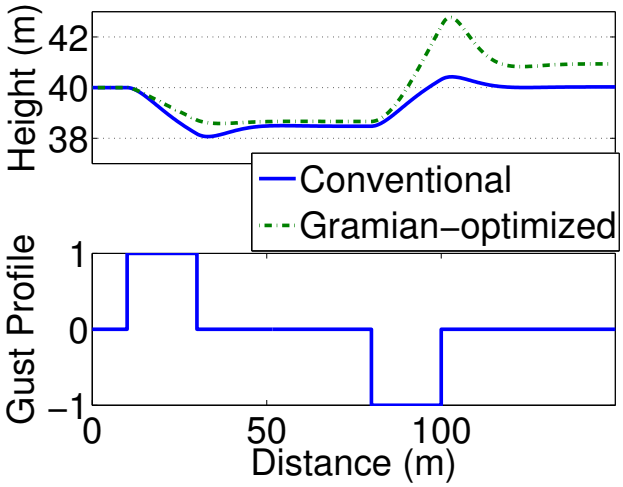

Figure 4.6: Flight trajectory over gust field for system (b).

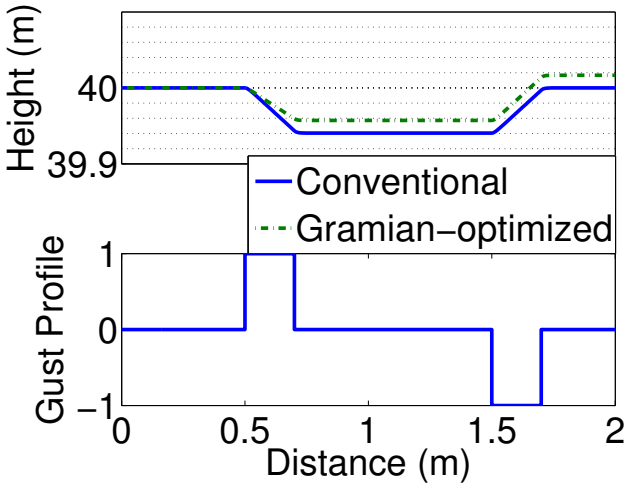

Figure 4.7: Flight trajectory over gust field for system (d).

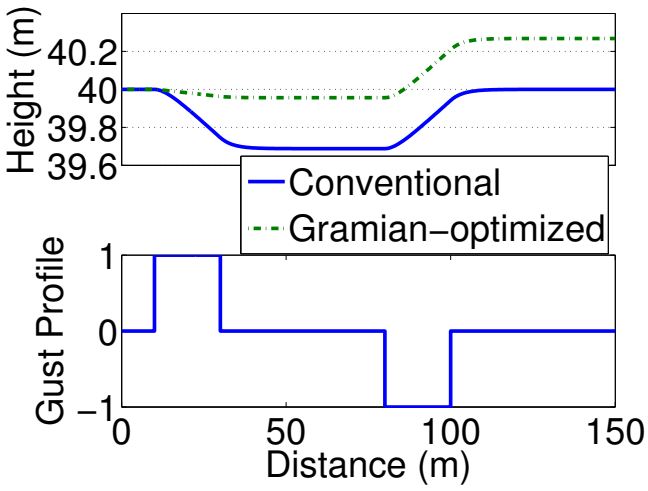

Figure 4.8: Flight trajectory over gust field for system (e).

4.3 Conclusion

This chapter presents a method of understanding the effect that gains in a linear static gain control approach have on the closed loop. This framework may be applied to design gust-aware flight controllers to understand and predict the relative sensitivities of flight control laws, and reduce our dependence on Monte-Carlo type simulations to study gust response of flight controllers. The gust capture metric as a basis for a gain scheduling control law to capture vertical gusts incorporates the disturbance gramian arising from the input gust and the corresponding observability gramian to maximize or minimize the disturbance in the applicable state. Using a unit norm gust to generate a disturbance gramian and a unit norm state to generate an observability gramian, the gust disturbance can be maximized or minimized in the desired direction. Gramian-aware control laws which are built on a theoretical formulation of closed loop gust response have potential for recovering atmospheric

energy and may be a method of enabling increases in mission endurance through feedback control. The formulation presented here, which accounts for the size of gust response via the determinant of the gust capture metric, that is composed of a disturbance and observability gramian, allows an a priori computation of the most and least gust sensitive gains within a closed loop control framework and provides a foundation for gust-scavenging flight control.

Chapter 5: Concluding Remarks

This thesis developed and presented a theoretical framework to achieve atmospheric energy recovery from the development of a gramian-aware control law that utilizes a a model of the vehicle dynamics. Energy recovery was quantified as net altitude gain from flying the UAV platform over vertical gust sections. A gust capture metric was defined accordingly and its volumetric size was presented as a direct quantification of the vehicle's sensitivity in the particular state to the particular gust disturbance. Univariate mapping of the gust capture metric's size was presented as proof of concept by modulating a sample vehicle Night Vapor's cruise speed condition. The importance of considering the observability gramian in conjunction with the disturbance gramian in a combined metric in the gust capture metric was highlighted from considering the various Apprentice model simulations as a function of cruise speed. The idea was then extended to the domain of ideal gain selection towards atmospheric energy harvesting. Here the physical intuition that was carried into the cruise speed example was lost. Once again initially the formulation was presented in detail with a univariate example of the fruitfly's hover dynamics, and subsequently it was noted that the same criterion of using volumetric size of the gust capture metric as a function of the scalar closed loop gain K was

validating the theory. Then this search was expanded into the multivariate form of gain-space across several different platforms. Again the simulations showed that the flights with the gramian-aware gain modulation were capturing more altitude or energy compared to a gramian-blind or constant-gain flight for the same platform. It is in these final set of results where it becomes apparent that application of this theory using the gust capture metric's size incorporating a platform's perturbability and observability can be expanded across the board to reach any and all modulations available to the controller of a UAV in flight.

Cruise speed and multivariate gain-space maps can easily be combined for an overall multivariate search for gust capture metric size over a combination of all these terms. Similarly, one may be able to add changing flight configuration via flaps or slats or modulating wing span or changing vehicle center of gravity or the steady-state angle of attack in rotorcraft to affect the gust capture metric size. All these can be considered individually or in tandem and made into a multivariate search by analogy to the multivariate gain-selection search examples. The application of the theory may also be expanded in a different direction, i.e. in considering different metrics as energy gain such as range extension. Appropriate selection of the observer matrix C will become a vital part of such an endeavour as range maximization is likely a joint function of more than one of the flight states, whereas altitude gain could be restricted to observing just the Δw state. Scaling the individual entries of C appropriately with vehicle size and speed becomes part of the challenge in this case. In the discussion on gain-selection in Chapter 4, C was scaled, albeit only in the vertical direction, using the size of the B matrix and mass and wingspan

of the vehicles. Similarly, expansions of this theory can be applied in the lateral sense, and simplified LTI models need not be the only baseline application either as nonlinear models and empirical gramians may be able to utilize the underlying theory. The issue of reaction time for the controller in relation to variant gust durations, magnitudes and turbulence may involve application of the developed theory on the non-steady-state gramians.

Bibliography

[1] Zhang, C., and Kovacs, J.M., "The application of small unmanned aerial systems for precision agriculture: a review", *Precision agriculture*, Vol. 13, No. 6, (2012), pp. 693-712.
doi: 10.1007/s11119-012-9274-5

[2] Jones, G.P., Pearlstine, L.G., and Percival, H.F., "An assessment of small unmanned aerial vehicles for wildlife research," *Wildlife Society Bulletin*, Vol. 34, No. 3, (2006), pp. 750-758.
doi: 10.2193/0091-7648(2006)34[750:AAOSUA]2.0.CO;2

[3] Lyon, D.H., "A military perspective on small unmanned aerial vehicles," *IEEE Instrumentation & Measurement Magazine*, Vol. 7, No. 3, (2004), pp. 27-31.
doi: 10.1109/MIM.2004.1337910

[4] Mulgaonkar, Y., Whitzer, M., Morgan, B., Kroninger, C.M., Harrington, A., and Kumar, V, "Power and Weight Considerations in Small Agile Quadrotors," *Proceedings of the Micro- and Nanotechnology Sensors, Systems, and Applications VI Conference Series*, Society of Photo-Optical Instrumentation Engineers (SPIE), Vol. 9083, Baltimore, MD, 2014.

[5] Ol, M., Parker, G., Abate, G. and Evers, J., "Flight controls and performance challenges for MAVs in complex environments," In *AIAA Guidance, Navigation and Control Conference and Exhibit*, 2008, pp. 6508.

[6] Frank H Gern, Daniel J Inman, and Rakesh K Kapania. Computation of Actuation Power Requirements for Smart Wings with Morphing Airfoils. AIAA Journal, 43(12), 2005.

[7] Ben T Dickinson. Hair receptor sensitivity to chainges in laminar boundary layer shape. BioInspiration and Biomimetics, 5(0116002), 2010.

[8] Mohamed, A., Watkins, S., Clothier, R., Abdulrahim, M., Massey, K., & Sabatini, R. (2014). Fixed-wing MAV attitude stability in atmospheric turbulence–Part 2: Investigating biologically-inspired sensors. Progress in Aerospace Sciences, 71, 1-13.

[9] Humbert, J.S., and Faruque, I.A., "Analysis of insect-inspired wingstroke kinematic perturbations for longitudinal control," *Journal of Guidance, Control, and Dynamics*, Vol. 34, No. 2, 2011, pp. 618-623.
doi: 10.2514/1.51912

[10] Dullerud, G.E., and Paganini, F., "Model Realizations and Reduction," *A Course in Robust Control Theory: A Convex Approach*, Springer, New York, NY, 2000, pp. 131-140.

[11] Gage, S., "Creating a unified graphical wind turbulence model from multiple specifications," *AIAA Modeling and simulation technologies conference and exhibit,* 2003.

[12] Sytsma, M.J., "Effects of turbulence on fixed wing small unmanned aerial systems," University of Florida, 2013.

[13] Etele, J., "Overview of wind gust modelling with application to autonomous low-level UAV control," Mechanical and Aerospace Engineering Department, Carelton University, Ottawa, Canada (2006).

[14] Zarovy, S.R., "Improved gust rejection for a micro coaxial helicopter in urban environments," Doctoral Dissertation, Georgia Institute of Technology, 2014.

[15] Golubev, V., Hollenshade, T., Nguyen, L. and Visbal, M., "High-Accuracy Low-Re Simulations of Airfoil-Gust and Airfoil-Vortex Interactions," In *40th Fluid Dynamics Conference and Exhibit*, 2010, pp. 4868.

[16] Watkins, S., Thompson, M., Loxton, B., and Abdulrahim, M., On Low Altitude Flight Through the Atmospheric Boundary Layer, *International Journal of Micro Air Vehicles*, Vol. 2, 2010, pp. 5568.

[17] "Beaufort Wind Scale. National Oceanic and Atmospheric Administration. http://www.spc.noaa.gov/faq/tornado/beaufort.html

[18] Habib, M., Quimby, P.W., Chang, S., Jackson, K. and Cummings, M.L., "Wind gust alerting for supervisory control of a micro aerial vehicle," In *Aerospace Conference*, 2011 IEEE, pp. 1-7.

[19] Langelaan, J.W., Alley, N. and Neidhoefer, J., "Wind field estimation for small unmanned aerial vehicles," *Journal of Guidance, Control, and Dynamics*, Vol. 34, No. 4, 2011, pp.1016-1030.

[20] Barbarino, S., Bilgen, O., Ajaj, R.M., Friswell, M.I. and Inman, D.J., "A review of morphing aircraft," *Journal of intelligent material systems and structures*, Vol. 22, No. 9, 2011, pp.823-877.

[21] Dillsaver, M., Cesnik, C. and Kolmanovsky, I., "Gust response sensitivity characteristics of very flexible aircraft," In *AIAA Atmospheric Flight Mechanics Conference*, 2012, pp. 4576.

[22] Oduyela, A. and Slegers, N., "Gust mitigation of micro air vehicles using passive articulated wings," *The Scientific World Journal*, 2014.

[23] Vance, J. T., Faruque, I., and Humbert, J.S., "Kinematic strategies for mitigating gust perturbations in insects," *Bioinspiration & biomimetics*, Vol. 8, No. 1, 2013.

[24] Bhatia, M., Patil, M., Woolsey, C., Stanford, B. and Beran, P., "Stabilization of flapping-wing micro-air vehicles in gust environments," *Journal of Guidance, Control, and Dynamics*, Vol. 37, No. 2, 2014, pp.592-607.

[25] Singh, V., Warren, L., Putnam, N., Walther, B., Becker, P., Danielson, A., Koraishy, B., Wood, W., Jensen, D. and Szmerekovsky, A., "A Novel Exploration Into Gust Resistant Operation of MAVs/UAVs Through Transformation," In *Second US-Euro MAV Conference*, Destin, FL, 2006.

[26] Hrishikeshavan, V., Benedict, M., and Chopra, I., "Identification of Flight Dynamics of a Cylcocopter Micro Air Vehicle in Hover", *Journal of Aircraft*, Vol. 52, No. 1 (2015), pp. 116-129.
doi: 10.2514/1.C032633

[27] Gardner, R. C., and Humbert, J. S. (2014). Comparative framework for maneuverability and gust tolerance of microhelicopters. Journal of Aircraft, 51(5), 1546-1553.

[28] Langelaan, J.W., "Gust Energy Extraction for Mini and Micro Uninhabited Aerial Vehicles", *Journal oF Guidance, Control, and Dynamics*; Vol. 32, No. 2, 2009, pp. 464-473.
doi: 10.2514/1.37735

[29] Langelaan, J.W., "Erratum: Gust Energy Extraction for Mini and Micro Uninhabited Aerial Vehicles", *Journal oF Guidance, Control, and Dynamics*; Vol.

34, No. 1, 2011, pp. 324-324.
doi: 10.2514/1.50149

[30] Patel, C.K., and Kroo, I.M., "Theoretical and Experimental Investigation of Energy Extraction from Atmospheric Turbulence," *Proceedings of the 26th International Congress of the Aeronautical Sciences,* AIAA, Anchorage, AK, 2008.

[31] Hamel, P.G. and Jategaonkar, R.V., "Evolution of flight vehicle system identification," *Journal of aircraft*, Vol. 33, No. 1, 1996, pp.9-28.

[32] Morelli, E.A., and Klein, V., "Application of system identification to aircraft at NASA Langley Research Center," *Journal of Aircraft*, Vol. 42, No. 1, 2005, pp. 12-25.

[33] Blake, W.B., "Missile Datcom: User's Manual-1997 FORTRAN 90 Revision," No. AFRL-VA-WP-TR-1998-3009, AIR FORCE RESEARCH LAB WRIGHT-PATTERSON AFB OH AIR VEHICLES DIRECTORATE, 1998.

[34] Drela, M. and Youngren, H., "Athena vortex lattice," Software Package, Ver, 3, 2004.

[35] Saxena, U., and Faruque, I., "Gramian-Inspired Unmanned Aerial Flight Control for Atmospheric Energy Capture," In *AIAA Atmospheric Flight Mechanics Conference*, 2016, pp. 3712.

[36] Dorobantu, A., Murch, A., Mettler, B., and Balas, G., "System Identification for Small, Low-Cost, Fixed-Wing Unmanned Aircraft," *Journal of Aircraft,* Vol. 50, No. 4, 2013, pp. 1117-1130.
doi: 10.2514/1.C032065

[37] Shields, M. and Mohseni, K., "Limitations of using the linearized equations of motion for MAV control," In *AIAA Guidance, Navigation, and Control Conference*, 2011, pp. 6221.

[38] Morelli, E.A., "Practical input optimization for aircraft parameter estimation experiments," National Aeronautics and Space Administration, Langley Research Center, 1993.

[39] Mehra, R., "Optimal inputs for linear system identification," *IEEE Transactions on Automatic Control*, Vol. 19, No. 3, 1974, pp.192-200.

[40] Schweppe, F. C., *Uncertain Dynamic Systems*, Prentice-Hall, New York, 1973.

[41] Horn, R.A., and Johnson, C.R., "Positive Definite Matrices," *Matrix Analysis*, Cambridge University Press, Melbourne, Australia 1985, pp. 407-408.

[42] Rugh, W.J., "Controllability and Observability," *Linear System Theory*, 2nd Ed., Prentice Hall, New Jersey, 1996, pp. 142-150.

[43] Himpe, C., "emgr-The Empirical Gramian Framework," arXiv preprint arXiv:1611.00675 (2016).

[44] Kailath, T., "Some Results for Time-Variant Systems," *Linear Systems*, Prentice-Hall, New Jersey, 1980, pp. 610-613.

[45] Chen, C., "Controllability and Observability," *Linear System Theory and Design*, 3rd Ed., Oxford University Press, 1999, pp. 143-158.

[46] Brown, R. G., "Not just observable, but how observable? Observability and controllability in providing heuristic understanding of control problems, noting Kalman filter theory," 22nd National Electronics Conference, CHICAGO, ILL. 1966.

[47] Monzingo, R., "A note on sensitivity of system observability," IEEE Transactions on Automatic Control, Vol. 12, No. 3, 1967, pp. 314-315.

[48] Kalman, R. E., Ho, Y. C., and Narendra, K. S., "Controllability of linear dynamical systems, Contributions to Differential Equations 1,", MR 155070, No. 27:5012, 1962, pp. 189-213.

[49] Mller, P. C., and Weber, H.I., "Analysis and optimization of certain qualities of controllability and observability for linear dynamical systems," *Automatica*, Vol. 8, No.3, 1972, pp. 237-246.

[50] Barth, N., "The gramian and k-volume in n-space: some classical results in linear algebra," Journal of Young Investigators 2, 1999.

[51] Beck, C., and D'Andrea, R., "Minimality, controllability and observability for uncertain systems" American Control Conference, Vol. 5, IEEE, 1997.
doi: 10.1109/ACC.1997.612035

[52] Hinamoto, T., Yokoyama, S., Inoue, T., Zeng, W., and Lu, W. S., "Analysis and minimization of L_2-sensitivity for linear systems and two-dimensional state-space filters using general controllability and observability Gramians," *IEEE Transactions on Circuits and Systems I: Fundamental Theory and Applications*, Vol. 49, No. 9, pp. 1279-1289.
doi: 10.1109/TCSI.2002.802362

[53] Marx, B., Koenig, D. and Georges, D., "Optimal sensor and actuator location for descriptor systems using generalized Gramians and balanced realizations," In *American Control Conference*, IEEE, Vol. 3, 2004, pp. 2729-2734.

[54] Shaker, H.R. and Tahavori, M., "Optimal sensor and actuator location for unstable systems," *Journal of Vibration and Control*, Vol. 19, No. 12, 2013, pp.1915-1920.

[55] Montagnier, P. and Spiteri, R.J., "A Gramian-based controller for linear periodic systems," *IEEE Transactions on Automatic Control*, Vol. 49, No. 8, 2004, pp.1380-1385.

[56] Szczublewski, D. P., *Gust disturbance analysis of a micro quadrotor helicopter*, MS Dissertation, 2012.

[57] Nelson, R.C., "Aircraft Response to Control or Atmospheric Inputs," *Flight Stability and Automatic Control,* 2nd ed., Vol. 2, WCB/McGraw Hill, Singapore, 1998, pp 217-218.

[58] Klein, V., and Morelli, E.A., "Regression Methods," *Aircraft System Identification: Theory and Practice,* American Institute of Aeronautics and Astronautics, Reston, VA, 2006, pp 95-97.

[59] Montgomery, D.C., Peck, E.A. and Vining, G.G., *Introduction to Linear Regression Analysis*, 3rd ed., Wiley, New York, 2001.

[60] Durbin, J., and Watson, G., "Testing for Serial Correlation in Least Squares Regression III", *Biometrika*, Vol. 58 No. 1 (1971), pp. 1-19.
doi: 10.2307/2334313

[61] Durbin, J., and Watson, G., "Testing for Serial Correlation in Least Squares Regression II", *Biometrika*, Vol. 38 No. 1-2 (1951), pp. 159-178.
doi: 10.1093/38.1-2.159

[62] Bendat, J.S., and Piersol, A.G., *Random Data Analysis and Measurement Procedures*, 2nd ed., Wiley, New York, 1986.

[63] Box, G.E.P., and Jenkins, G.M., *Time Series Analysis: Forecasting and Control*, Holden-Day, San Francisco, 1976.

[64] Fluent, "7.2.2 Determining Turbulence Parameters," *Ansys. 12.0 User Guide. User Inputs for Porous Media 6*, 2009.

[65] Farouk, M.I., Mourad, S.A., and Salaheldin, A.S., "Numerical simulation of wind effects on an airport air traffic control tower," emphFluid Structure Interaction and Moving Boundary Problems IV, No. 92, 2007, pp.183.

[66] Kalman, R.E., "Contributions to the Theory of Optimal Control," *Boletin de la Sociedad Matematica Mexicana,* Vol. 5, No. 2, 1960, pp. 102-119.

[67] Saxena, U., and Faruque, I. A., "Theoretical Model for the Gust Performance of Closed-Loop Flight Control," *Journal of Guidance, Control, and Dynamics*, 2017.

[68] Hrishikeshavan, V., Humbert, J.S., and Chopra, I., "Gramian Analysis of a Shrouded Rotor Micro Air Vehicle in Hover," *Journal of Guidance, Control, and Dynamics,* Vol. 37, No. 5, 2014, pp. 1684-1691.
doi: 10.2514/1.G000066